PGC-1α drives small cell neuroendocrine cancer progression towards an ASCL1-expressing subtype with increased mitochondrial capacity

Grigor Varuzhanyan[1,**], Chia-Chun Chen[2], Jack Freeland[2,3], Tian He[2], Wendy Tran[1], Kai Song[4], Liang Wang[1], Donghui Cheng[5], Shili Xu[2,7,12], Gabriella A. Dibernardo[5,10], Favour N Esedebe[6], Vipul Bhatia[15,16], Mingqi Han[14], Evan R. Abt[2], Jung Wook Park[8], Sanaz Memarzadeh[9,10,11,12,13], David Shackelford[12,14], John K. Lee[15,16], Thomas Graeber[2,5,7,12,17,18], Orian Shirihai[2,3,19,20], Owen Witte[1,2,5,12,13,21,*]

1. Department of Microbiology Immunology and Molecular Genetics, University of California, Los Angeles (UCLA), CA, USA
2. Department of Molecular and Medical Pharmacology, UCLA, CA, USA
3. Molecular Biology Interdepartmental Program, UCLA, CA, USA
4. Department of Bioengineering, UCLA, CA, USA
5. Eli and Edythe Broad Stem Cell Research Center, UCLA, CA, USA
6. Bioinformatics Interdepartmental Program, UCLA, CA, USA
7. Crump Institute for Molecular Imaging, David Geffen School of Medicine, UCLA, CA, USA
8. Department of Pathology, Duke University School of Medicine, Durham, NC, USA
9. Eli and Edythe Broad Center of Regeneration Medicine and Stem Cell Research, UCLA, CA, USA
10. Department of Obstetrics and Gynecology, David Geffen School of Medicine, UCLA, CA, USA
11. The VA Greater Los Angeles Healthcare System, Los Angeles, CA, USA
12. Jonsson Comprehensive Cancer Center, the David Geffen School of Medicine, UCLA, CA, USA
13. Molecular Biology Institute, UCLA, CA, USA
14. Pulmonary and Critical Care Medicine, David Geffen School of Medicine (DGSOM), UCLA, CA, USA.
15. Division of Hematology/Oncology, Department of Medicine UCLA Jonsson Comprehensive Cancer Center, Los Angeles, CA, 90095, USA
16. Human Biology Division, Fred Hutchinson Cancer Center, 1100 Fairview Ave N, Seattle, WA, 98109, USA
17. California NanoSystems Institute, UCLA, CA, USA
18. Metabolomics Center, UCLA, CA, USA
19. Division of Endocrinology, Department of Medicine, David Geffen School of Medicine, UCLA, CA 90095, USA
20. Department of Clinical Biochemistry, School of Medicine, Ben Gurion University of The Negev, Beer-Sheva, Israel
21. Parker Institute for Cancer Immunotherapy, UCLA, CA, USA

Corresponding Author Emails

*Owen N. Witte: owenwitte@mednet.ucla.edu

**Grigor Varuzhanyan: gvaruzhanyan@mednet.ucla.edu

Keywords: PGC-1α; ASCL1; ASCL2; POU2F3; OXPHOS; lineage plasticity; small cell neuroendocrine; prostate cancer; lung cancer

ABSTRACT

Adenocarcinomas from multiple tissues can evolve into lethal, treatment-resistant small cell neuroendocrine (SCN) cancers comprising multiple subtypes with poorly defined metabolic characteristics. The role of metabolism in directly driving subtype determination remains unclear. Through bioinformatics analyses of thousands of patient tumors, we identified enhanced PGC-1α—a potent regulator of oxidative phosphorylation (OXPHOS)—in various SCN cancers (SCNCs), closely linked with neuroendocrine differentiation. In a patient-derived prostate tissue SCNC transformation system, the ASCL1-expressing neuroendocrine subtype showed elevated PGC-1α expression and increased OXPHOS activity. Inhibition of PGC-1α and OXPHOS reduced the proliferation of SCN lung and prostate cancer cell lines and blocked SCN prostate tumor formation. Conversely, enhancing PGC-1α and OXPHOS, validated by small-animal Positron Emission Tomography mitochondrial imaging, tripled the SCN prostate tumor formation rate and promoted commitment to the ASCL1 lineage. These results establish PGC-1α as a driver of SCNC progression and subtype determination, highlighting novel metabolic vulnerabilities in SCNCs across different tissues.

STATEMENT OF SIGNIFICANCE

Our study provides functional evidence that metabolic reprogramming can directly impact cancer phenotypes and establishes PGC-1α-induced mitochondrial metabolism as a driver of SCNC progression and lineage determination. These mechanistic insights reveal common metabolic vulnerabilities across SCNCs originating from multiple tissues, opening new avenues for pan-SCN cancer therapeutic strategies.

INTRODUCTION

Epithelial cancers from various tissues, including the prostate, lung, and bladder, can converge to an aggressive small cell neuroendocrine (SCN) phenotype under targeted treatments[1–3]. These phenotypically similar, small cell neuroendocrine cancers (SCNCs) are classified as high-grade, poorly differentiated small cell carcinomas that commonly express neuroendocrine markers like chromogranin A (CHGA), neural cell adhesion molecule 1 (NCAM1), and synaptophysin (SYP)[4]. Small cell lung cancer (SCLC), the most prevalent type of SCNC, represents about 14% of all lung cancer diagnoses, with approximately 200,000 patients succumbing to the disease annually. The prevalence of treatment-induced SCN prostate cancer, which accounts for approximately 10-40% of all androgen deprivation therapy (ADT)-insensitive, castration-resistant prostate cancer (CRPC) cases, is increasing, likely due to resistance mechanisms ADT. With a limited long-term effectiveness of current chemotherapy strategies[5] indicated by a dismal median survival rate between 7-16 months[6], there is a pressing need for a better mechanistic understanding of disease progression to inform new therapeutic strategies.

SCNCs were traditionally seen as a uniform group of cancers but are now understood to include multiple subtypes. These subtypes, defined by their prominent expression of lineage-specific molecular markers, showcase the diversity within SCNCs. This is best exemplified in SCLC, which is categorized into ASCL1, NEUROD1, POU2F3, and YAP1 subtypes[7,8]. Recent studies have identified corresponding subtypes in SCN prostate cancer, including ASCL1, POU2F3/ASCL2, and NEUROD1[9–11]. A growing body of research across numerous SCNC models has highlighted the plastic nature of differentiation towards and between these subtypes[7,8,12–14], a feature that likely contributes to treatment resistance.

Complementing the molecular heterogeneity within SCNCs, recent studies have begun to highlight the metabolic diversity across different SCLC subtypes[15–19]. Further, a correlation has been observed between ASCL1 expression levels and a dependence on inosine monophosphate dehydrogenase, a key enzyme in guanosine biosynthesis critical for normal metabolic functions[15]. These insights raise the possibility that metabolic reprogramming might regulate lineage plasticity in SCNCs. Indeed, metabolic reprogramming not only influences cell fate decisions[20] but is also orchestrated by oncogenes to regulate these decisions[21]. These observations highlight the intimate interplay between

91 cancer metabolism and lineage plasticity. SCN-associated oncogenes such as MYC[22–26], AKT[27,28],
92 TP53[29,30], and RB1[31–33], regulate metabolic pathways individually, but their collective impact on metabolic
93 reprogramming and lineage determination during SCNC remains unclear.

94 A key aspect of cancer cell metabolic reprogramming is the shift towards aerobic glycolysis (also
95 known as the Warburg effect) characterized by an increased rate of glucose consumption and lactate
96 secretion, even in the presence of ample oxygen[34–36]. This seminal discovery made nearly a century ago
97 by Otto Warburg led to a longstanding belief that cancer cells have dysfunctional mitochondria. However,
98 recent studies have countered this perspective, showing that many cancers actually have functional
99 mitochondria fully capable of processing fuels via the tricarboxylic acid (TCA) cycle to support oxidative
100 phosphorylation (OXPHOS)[37]. In fact, some cancers have a heightened reliance on OXPHOS[38,39], which
101 is sometimes linked with therapy resistance[40–45]. This emerging understanding has sparked significant
102 interest in OXPHOS inhibitors as promising candidates for cancer therapy[46–48]. However, their utility in
103 treating SCNCs remains unclear owing to an incomplete understanding of the metabolic dynamics in
104 these aggressive cancers. Although increased aerobic glycolysis has been observed in SCN prostate
105 cancer[49], the OXPHOS status in SCNCs and their subtypes remains unclear. Therefore, we reasoned
106 that exploring mitochondrial function in SCNCs may reveal pivotal insights into their pathophysiology

107 To explore the influence of mitochondrial function on SCNC development, we focused on
108 peroxisome proliferator-activated receptor gamma coactivator 1-alpha (PGC-1α)[50], a transcriptional co-
109 activator widely recognized as a potent regulator of mitochondrial biogenesis and OXPHOS. Originally
110 identified for its role in cold-induced adaptive thermogenesis through the regulation of OXPHOS genes[51],
111 PGC-1α has since been implicated in metabolic reprogramming during cancer development,
112 demonstrating robust but varied effects across cancer types[52]. In prostate cancer, it has been found to
113 support the growth of localized, androgen-dependent tumors[53,54] while restraining the progression of
114 androgen-independent, metastatic forms[55–57]. In melanoma, PGC-1α is associated with tumors that
115 exhibit enhanced mitochondrial function[58] and a reduced metastatic potential[59]. It suppresses metastasis
116 in non-small cell lung cancer (NSCLC)[60], but promotes metastasis in other cancer models[61]. These
117 observations demonstrate that while the exploration of PGC-1α has yielded critical insights into cancer

118 metabolism and progression, its influence is context-dependent. Therefore, unraveling the specific effects
119 of PGC-1α in SCNCs could provide key insights into potential therapeutic targets or prognostic factors.
120 To investigate the role of PGC-1α in regulating SCNC development, we performed an integrated
121 computational and functional investigation. Bioinformatics analyses of 10,529 patient tumors and 1,466
122 human cancer cell lines were performed, followed by functional and mechanistic analyses using multiple
123 model systems including a human prostate tissue-derived SCN transformation system, referred to as
124 PARCB[2,3,11]. This system enables the transformation of normal human lung epithelial cells, prostate
125 epithelial cells, or bladder urothelial cells into SCNC via transduction with an oncogene cocktail
126 abbreviated as PARCB (TP53DN, myr-AKT, shRB1, c-MYC, and BCL2). This model generates two
127 distinct tumor lineages characterized by either stem-like (POU2F3/ASCL2 subtype) or neuroendocrine
128 features (ASCL1 subtype) that closely resemble the POU2F3 and ASCL1 subtypes seen in clinical
129 SCNCs[11]. Here, we reveal the metabolic heterogeneity among SCNC subtypes, defined by PGC-1α and
130 OXPHOS levels. We also identify PGC-1α as a driver in the ASCL1 lineage and uncover OXPHOS as a
131 broad metabolic vulnerability across SCNCs originating from multiple tissues.
132
133 **RESULTS**
134 Elevated PGC-1α in clinical SCNC correlates with increased ASCL1 expression and neuroendocrine
135 differentiation.
136 To investigate the role of mitochondrial metabolism in SCNCs, we started by conducting
137 bioinformatics analyses in a wide range of human cancer cell lines, human primary tumors, and clinical
138 SCN datasets. First, a co-expression analysis was conducted on PGC-1α against the four SCNC lineage
139 markers—ASCL1, POU2F3, NEUROD1, and YAP1—across all 1,466 human cancer cell lines from the
140 Cancer Cell Line Encyclopedia (CCLE). While PGC-1α does not correlate with POU2F3, NEUROD1, or
141 YAP1 (**Figure S1A**), it shows significant positive correlation with the lineage marker ASCL1, a pioneer
142 transcription factor that is essential for neuronal commitment and SCNC progression[62–64] (**Figure 1A**).
143 Notably, we observed a distinct subpopulation of cell lines with high ASCL1 expression that also have
144 high PGC-1α expression (**Figure 1A, left panel**). We refer to this subpopulation as "PGC-1α/ASCL1-

145 High." To determine the cancer type composition of the PGC-1α/ASCL1-High subpopulation compared
146 to the rest of the samples, we quantified the percentage of cell lines with SCN features in both groups.
147 The PGC-1α/ASCL1-High subpopulation is predominantly comprised of SCNCs (54/68, 79%) (**Figure**
148 **1A right panel**), whereas only a small fraction of the rest of the cells (88/1466, 6%) are SCNCs.
149 Consistently, PGC-1α expression is elevated in SCLC and neuroblastoma cell lines (two cancers with
150 SCN differentiation) compared with NSCLC, which typically does not exhibit SCN differentiation (**Figure**
151 **S1B**). These observations suggest that PGC-1α and ASCL1 are co-upregulated in SCNCs from multiple
152 tissues.

153 To determine whether PGC-1α/ASCL1-High cells show increased SCN differentiation, we applied
154 a well-established SCN score derived from a pan-cancer transcriptomic analysis[1], where a higher SCN
155 score indicates a more SCN-like phenotype (see the Methods section for more details). PGC-1α/ASCL1-
156 High cells from the CCLE show a marked increase in SCN score compared to the rest of the samples,
157 indicating heightened SCN differentiation. (**Figure 1B**). Together, these data uncover a hitherto
158 uncharacterized link between PGC-1α and ASCL1.

159 To determine whether the link between PGC-1α, ASCL1, and SCN differentiation extends beyond
160 cultured cell lines to patient tumors, we analyzed 10,529 solid tumors from The Cancer Genome Atlas
161 (TCGA)[65]. Consistent with findings from the cancer cell lines, co-expression analysis identified a distinct
162 subpopulation of PGC-1α/ASCL1-High tumors (**Figure S1C**), which exhibited a robust increase in SCN
163 score (**Figure 1C**). We then expanded the analysis to include clinical SCN samples from various cancers,
164 including lung adenocarcinoma (LUAD), castration-resistant prostate cancer (CRPC), SCN prostate
165 cancer (NEPC), and small cell lung cancer (SCLC)[66–69]. Similar to the patterns observed in the CCLE cell
166 lines and TCGA patient tumors, the majority of clinical samples with increased ASCL1 expression also
167 showed high PGC-1α expression (**Figure 1D, left panel)**. Moreover, most PGC-1α/ASCL1-High patient
168 samples were cancer types that display neuroendocrine or small cell features (56/83; 67%) and had a
169 substantial increase in SCN score (**Figure 1D, right panel**). Consistent with these observations, PGC-
170 1α expression is increased in SCN prostate cancer compared with castration resistant prostate cancer
171 (CRPC)[66] and in SCLC[70] compared with NSCLC[65] (**Figure S1D**). Thus, as in the CCLE cell lines and

172 TCGA tumors, PGC-1α and ASCL1 are co-upregulated in clinical tumors with heightened SCN
173 differentiation. Of note, the increased PGC-1α expression in SCLC is largely attributable to the
174 neuroendocrine subtype expressing ASCL1 (SCLC-A), further substantiating the link between PGC-1α
175 and ASCL1 (**Figure S1D, right panel**).

176 Epithelial ovarian cancers, particularly high-grade serous ovarian carcinomas (HGSOC), share
177 genomic alterations with neuroendocrine tumors including mutations in TP53, loss of RB1, and
178 amplification of MYC[71]. We therefore examined expression of PGC-1α and its correlation with ASCL1 in
179 a cohort of patients with a diagnosis of HGSOC, drawing on data from our unpublished research. A
180 positive correlation between PGC-1α and ASCL1 was observed in this cohort (**Figure S1E**), highlighting
181 a consistent link across multiple clinical sample types.

182 Given the known contribution of ADT to SCN prostate cancer progression[72,73], we next examined
183 the effect of ADT on PGC-1α expression in clinical prostate cancer (**Figure 1E**). A clinical transcriptomic
184 dataset was utilized in which tumors were biopsied from the same prostate cancer patients before and
185 after ADT with enzalutamide, a potent and selective antagonist of the androgen receptor[74]. ADT-treated
186 tumors show increased PGC-1α expression, which positively correlates with ASCL1, consistent with our
187 analyses of CCLE, TCGA, and clinical SCNC datasets (**Figure S1F**). To identify enriched pathways upon
188 ADT treatment, we performed gene set enrichment analysis (GSEA) on patient samples before and after
189 ADT. Consistent with the increased PGC-1α expression, this GSEA revealed OXPHOS as a top enriched
190 pathway in post-ADT tumors (**Figure 1E**). As expected, the Androgen Response pathway is a top
191 downregulated pathway in patient tumors post-ADT (**Figure 1E**). Collectively, these data indicate that
192 PGC-1α expression is upregulated in multiple SCNCs and uncover a previously undescribed link between
193 PGC-1α, ASCL1, and SCN differentiation.

194

195 <u>Enhanced PGC-1α expression and OXPHOS activity in SCN prostate cancer within the ASCL1 tumor</u>
196 <u>subtype.</u>

197 Having established a link between PGC-1α and ASCL1 in multiple clinical SCNCs, we next sought
198 to investigate the functional role of PGC-1α in specific SCNCs subtypes. With this goal in mind, we utilized

199 our human tissue-derived PARCB-induced SCN transformation model[11]. This model produces ASCL1
200 and POU2F3/ASCL2 subtypes, closely resembling clinical SCLC and SCN prostate cancer subtypes
201 (**Figure 2A**). To determine if PGC-1α is linked to the ASCL1 subtype in the PARCB model, we conducted
202 a co-expression analysis across all PARCB time course samples. This analysis revealed a tight and
203 positive correlation between PGC-1α and ASCL1, with the highest expression of both genes exclusively
204 found in the ASCL1 subtype (**Figure 2B**). Corroborating this observation, PGC-1α expression markedly
205 increased in five out of ten PARCB tumor series derived from distinct donor tissue series (**Figure 2C**).
206 Moreover, across all the patient series, the ASCL1 neuroendocrine subtype demonstrated a 16-fold
207 higher expression of PGC-1α compared with the POU2F3/ASCL2 subtype (**Figure 2D)**. To check
208 whether PGC-1α and ASCL1 are co-expressed at the single cell level, we examined single-cell RNA-
209 sequencing (scRNA-seq) from the same PARCB time course dataset[11]. The analysis revealed that high
210 PGC-1α expression was almost exclusively associated with ASCL1, while it was absent in cells
211 expressing POU2F3 or ASCL2 (**Figure 2E**). Collectively, these data indicate increased PGC-1α
212 expression in the ASCL1 subtype, which aligns with the bioinformatics analyses in patient tumors and
213 clinical datasets described in Figure 1.

214 Building on our findings that PGC-1α expression is elevated in the ASCL1 tumor subtype, we
215 further investigated the regulatory mechanisms underlying this phenomenon. Specifically, we aimed to
216 determine if transcription factors (TFs) co-activated by PGC-1α are more accessible in the ASCL1
217 subtype than in the POU2F3/ASCL2 subtype. Hypergeometric Optimization of Motif EnRichment
218 (HOMER) analysis was performed to compare the accessible peaks in both tumor subtypes. In the
219 ASCL1 tumor subtype, there was a notable enrichment of transcription factors co-activated by PGC-1α,
220 including HNF4 and PPPARA, which were among the most significantly enriched (**Figure S2**). This
221 enrichment suggests enhanced PGC-1α-induced TF signaling in the ASCL1 subtype, further
222 corroborating the link between PGC-1α and ASCL1.

223 Given the shared molecular alterations driven by a common set of oncogenes in both ASCL1 and
224 POU2F3/ASCL2 subtypes, we investigated whether ASCL1, as a pioneer transcriptional activator, could
225 directly interact with PGC-1α gene promoters to enhance its expression specifically in the ASCL1

226 subtype. We analyzed ASCL1 ChIP-Seq datasets from SCN lung[75,76] and prostate cancer cell lines[63,77],
227 as well as in LuCaP prostate cancer patient-derived xenografts (PDXs)[10]. ASCL1's binding to an
228 alternative promoter of PGC-1α, particularly at exon 1b[78] encoding transcript variant X2
229 (XM_005248132.1), was modest in SCN lung and prostate cancer cell lines but absent in prostate cancer
230 PDX models (**Figure S3**). In contrast, prostate cancer PDX models showed ASCL1 with a stronger affinity
231 for variant 1 (NM_001330751.2) of PGC-1α, a pattern not observed in SCN lung and prostate cancer cell
232 lines (**Figure S4**). Additionally, ASCL1's interaction within the PGC-1α gene body was exclusive to SCN
233 lung cancer cell lines and was not present in SCN prostate cancer cell lines and PDX models (**Figure**
234 **S5**). These inconsistent binding patterns across datasets and models hinder definitive conclusions about
235 ASCL1's direct regulation of PGC-1α.

236 Given our findings of variable ASCL1 binding to PGC-1α DNA, we sought to determine if a
237 functional connection exists that does not solely rely on direct DNA interaction. To this end, we
238 investigated whether exogenous ASCL1 expression could upregulate PGC-1α. Analyzing data from our
239 previous study[11], we found that ASCL1 overexpression in two PARCB POU2F3/ASCL2 tumor-derived
240 cell lines, which naturally do not express PGC-1α, led to increased PGC-1α expression in both cell lines
241 (**Figure S6A**). This enhancement of PGC-1α expression by ASCL1 suggests that ASCL1 can regulate
242 PGC-1α expression even in cells that naturally lack it.

243 Given our findings of variable ASCL1 binding to PGC-1α DNA, we sought to determine if a
244 functional connection exists that does not solely rely on direct DNA interaction. TO this end we examined
245 whether exogenous expression of ASCL1 could upregulate PGC-1α. We analyzed data from our prior
246 study where ASCL1 was overexpressed in two PARCB POU2F3/ASCL2 tumor-derived cell lines, which
247 do not express PGC-1α[11] (**Figure S6A**). ASCL1 overexpression enhanced the expression of PGC-1α in
248 both cell lines (**Figure S6A**), indicating that it can regulate PGC-1α expression.

249 To ensure that ASCL1's regulatory effect on PGC-1α extends beyond the PARCB cell lines, we
250 utilized a newly developed in vitro model for SCN prostate cancer differentiation using the androgen-
251 insensitive C4-2B cell line[77]. This model induces SCN differentiation by incorporating a specific set of
252 SCN oncogenes and transcription factors, namely PRNBSAN (dominant-negative TP53, shRB1, MYCN,

253 BCL2, SRRM4 combined with ASCL1, or NEUROD1) (**Figure S6B**). Consistent with findings in the
254 PARCB cell lines, we observed a strong correlation between PGC-1α and ASCL1 expression, evidenced
255 by an R^2 value of 0.9059 (**Figure 2F**). Moreover, PGC-1α levels correlated with enhanced SCN
256 differentiation in this model (**Figure S6C**). Collectively, these findings across multiple model systems
257 establish ASCL1 as a positive regulator of PGC-1α expression and reinforce the functional connection
258 between PGC-1α, ASCL1, and neuroendocrine differentiation.

259 Following our demonstration of both a tight correlative and functional link between ASCL1 and
260 PGC-1α, we proceeded to define the transcriptional changes associated with the development of the
261 ASCL1 subtype. GSEA was performed in tumors of the ASCL1 subtype versus all the other stages of
262 PARCB transformation (**Figure 2G**). Consistent with their high PGC-1α expression, ASCL1 tumors had
263 pronounced upregulation of oxidative phosphorylation (OXPHOS) genes (**Figure 2G**), indicating
264 increased mitochondrial biogenesis and/or activity. To determine whether the increased OXPHOS
265 expression translated to higher OXPHOS activity, we performed respirometry using a Seahorse XF
266 Analyzer (Agilent Technologies). This extracellular flux analysis utilizes multiple inhibitors targeting
267 different components of the OXPHOS machinery, providing a detailed functional profile of OXPHOS
268 activity[79]. Seahorse respirometry revealed that PARCB-ASCL1 tumor-derived cell lines exhibited a
269 marked increase in basal and maximal oxygen consumption rates (**Figure 2H**), indicating increased
270 OXPHOS activity compared with the POU2F3/ASCL2 subtype. Furthermore, the ASCL1 tumor subtype
271 had higher expression of both subunits of the mitochondrial pyruvate carrier (MPC) (**Figure S6D**), an
272 obligate heterodimer in the mitochondrial inner membrane that allows entry of pyruvate into the
273 mitochondrion to fuel OXPHOS[80]. Collectively, these findings demonstrate that the ASCL1 subtype
274 exhibits enhanced PGC-1α expression and OXPHOS activity.

275

276 PGC-1α inhibition blunts OXPHOS, reduces the growth of SCNC cell lines, and blocks SCN prostate
277 tumor formation.

278 Considering the increased PGC-1α expression in SCNCs described in Figures 1 and 2, we next
279 asked whether PGC-1α is important for PARCB tumor progression. PGC-1α was inhibited during PARCB

280 prostate transformation using shRNA interference (**Figure S7A**). PGC-1α inhibition was verified using
281 RT-qPCR in PARCB organoids before xenografting into immunocompromised mice for tumor formation
282 (**Figure S7B**). PGC-1α inhibition blocked PARCB tumor growth, underscoring its requirement for PARCB
283 prostate tumor initiation.

284 Since PARCB tumors could not form under PGC-1α inhibition, we explored its role in the
285 proliferation of PARCB tumor derived prostate cancer cell lines. PGC-1α inhibition reduced the
286 proliferation of both ASCL1 and POU2F3/ASCL2 subtypes with a more pronounced effect in the latter
287 (**Figures 3A**). Next, we examined whether pharmacological inhibition of PGC-1α similarly affects cell
288 proliferation. A recent high-throughput screen identified a small molecule inhibitor called SR-18292 that
289 increases PGC-1α lysine acetylation and inhibits PGC-1α activity by blocking its interaction with HNF4A[81].
290 As with genetic inhibition, SR-18292 treatment suppressed growth in both ASCL1 and POU2F3/ASCL2
291 subtypes, with a stronger effect on the POU2F3ASCL2 subtype (**Figure 3B**).

292 To determine whether this effect of PGC-1α inhibition extends beyond the PARCB-derived cell
293 lines, we first examined its effect on PRNBSA-induced SCN prostate cancer progression (model
294 described in Figure 2C). PGC-1α inhibition using shRNA, blocked the PRNBSA-mediated growth of C4-
295 2B and LNCaP cell lines (**Figure S7C and S7D**). Next, we tested the effect of PGC-1α inhibition on
296 patient-derived SCN prostate and lung cancer cell lines. PGC-1α inhibition reduced the growth of the sole
297 patient-derived SCN prostate cancer cell line, NCI-H660 (**Figure 3C**). Similarly, analysis of PGC-1α
298 inhibition in the Cancer Dependency Map (DepMap)[82] revealed a stronger anti-proliferative effect in
299 SCLC compared with NSCLC (**Figure 3D**). Taken together, these findings indicate that PGC-1α inhibition
300 blunts the growth of both SCN prostate and lung cancer cell lines.

301 We next sought to understand the functional mechanism behind PGC-1α inhibition's impact on
302 SCNC cell line growth and PARCB tumor suppression. We noted in Figure 2 above that the ASCL1
303 subtype has enhanced PGC-1α expression and OXPHOS activity. We therefore examined whether PGC-
304 1α inhibition would blunt OXPHOS in SCN prostate cancer cell lines. Accordingly, we inhibited PGC-1α
305 in ASCL1 and POU2F3/ASCL2 cell lines using shRNA and performed Seahorse respirometry to examine
306 the effect on mitochondrial function. PGC-1α inhibition downregulated basal and maximal respiration in

307 both the ASCL1 and POU2F3/ASCL2 subtypes (**Figure 3E**), highlighting the importance of PGC-1α in
308 maintaining OXPHOS activity across both subtypes. These findings collectively suggest that PGC-1α is
309 essential for the initiation of PARCB prostate tumors and sustaining OXPHOS and proliferation of cultured
310 SCNC cell lines.
311
312 <u>OXPHOS inhibition blunts SCN prostate and lung cancer cell line proliferation.</u>
313 Because PGC-1α inhibition blunted OXPHOS and reduced the growth of SCN prostate and lung
314 cancer cells, we tested whether OXPHOS is required for the proliferation of SCNC cell lines. First, PARCB
315 cell lines derived from the ASCL1 and POU2F3/ASCL2 tumor subtypes were treated with IMT1B, a
316 recently developed small molecule inhibitor of mitochondrial RNA polymerase (POLRMT), which blocks
317 mitochondrial DNA transcription thereby downregulating all of the mitochondrially-encoded respiratory
318 chain complexes[83]. IMT1B treatment blunted cell proliferation in both SCN prostate and lung cancer cell
319 lines with approximately twice the potency in the POU2F3/ASCL2 subtype (**Figure 4A**).
320 We next examined the effect of OXPHOS gene deletion in SCN lung cancer by investigating
321 genetic dependencies of 104 lung cancer cell lines in the DepMap database. We first performed
322 unsupervised principal component analysis (PCA) using the DepMap dependency scores. There was a
323 distinct separation between SCLC and NSCLC samples (**Figure 4B, left panel**), indicating unique
324 genetic dependencies between the two groups. Pathway enrichment analysis from the top and bottom
325 100 PC1 loading genes indicated that OXPHOS is a top enriched pathway in SCLC versus NSCLC
326 cancer cell lines, implying that OXPHOS gene deletion has a stronger anti-proliferation effect in SCLC
327 versus NSCLC (**Figure 4B, right panel**).
328 Having established that OXPHOS inhibition, through gene deletion or mt-DNA transcription
329 inhibition with IMT1B, reduces SCNC proliferation, we utilized an alternative approach by employing a
330 clinical-grade respiratory chain complex I inhibitor, IACS-010759. This method offered another avenue
331 to explore OXPHOS suppression in SCN prostate and lung cancer cell lines, under conditions that mimic
332 potential clinical interventions. This treatment abolished OXPHOS in cell lines derived from both subtypes
333 (**Figure 4C**). To confirm the inhibitor's specificity and ensure that the observed effects were directly due

334 to complex I inhibition, NDI1, a yeast complex I[47,84] was overexpressed concurrently with complex I
335 inhibition**.** NDI1 overexpressed fully rescued the OXPHOS inhibition caused by IACS-010759 (**Figure**
336 **4C**). Interestingly, NDI1 overexpression boosted the oxygen consumption rate (OCR) above baseline
337 levels only in the ASCL1 subtype (**Figure 4C**), suggesting that this subtype not only has increased
338 OXPHOS activity but may also have higher metabolic plasticity compared to the POU2F3/ASCL2
339 subtype.

340 Having verified that IACS-010759 blocks OXPHOS in these SCN prostate cell lines, we next
341 asked whether its treatment would reduce their proliferation in culture. In line with the PGC-1α and
342 OXPHOS inhibition experiments described above, IACS-010759 treatment reduced proliferation of cell
343 lines derived from both subtypes, with a more pronounced effect in the POU2F3/ASCL2 subtype (**Figure**
344 **4D**). These anti-proliferation effects caused by IACS-010759 were fully rescued by NDI1 overexpression
345 (**Figure 4D**), indicating high specificity of the inhibitor. A similar anti proliferation effect was observed in
346 SCN lung cancer cell lines, with a more pronounced effect in the POU2F3 subtype (**Figure 4D**).
347 Collectively, these results indicate that PGC-1α and OXPHOS inhibition are critical metabolic
348 vulnerabilities in SCN cancers of both the prostate and lung.

349

350 <u>PGC-1α promotes OXPHOS in the prostate cancer ASCL1 subtype.</u>

351 As described above in Figure 3E, PGC-1α inhibition reduced OXPHOS activity in SCNC cell lines.
352 Could overexpressing PGC-1α, therefore, be sufficient to promote OXPHOS and induce lineage
353 plasticity? To test this, we generated a lentiviral PGC-1α overexpression construct for stable transduction.
354 First, PGC-1α overexpression was verified using western blot analysis in a panel of PARCB prostate
355 cancer cell lines generated previously[2]. As expected, PGC-1α overexpression increased both PGC-1α
356 and OXPHOS protein levels in these cell lines (**Figure S8A**). Next, PGC-1α was overexpressed in
357 POU2F3/ASCL2 and ASCL1 PARCB tumor-derived cell lines, and its effect on OXPHOS activity and
358 neuroendocrine differentiation were measured. This analysis utilized Seahorse respirometry, followed by
359 in vivo micro positron emission tomography (PET) and computed tomography (microPET/CT) imaging,
360 and histological analyses **(Figure 5A)**. PGC-1α overexpression upregulated OXPHOS activity in cell lines

361 derived from the ASCL1 but not POU2F3/ASCL2 subtype (**Figure 5B**). This result is consistent with the
362 ASCL1 subtype's selective OXPHOS enhancement from yeast Complex I overexpression seen in Figure
363 4A, suggesting a relatively flexible metabolic state in the ASCL1 subtype.

364 To check whether the increased OXPHOS caused by PGC-1α overexpression in cell lines would
365 translate to higher bioenergetics in tumors, ASCL1 or POU2F3/ASCL2 cell lines with and without PGC-
366 1α overexpression were xenografted into immunocompromised mice for tumor initiation and subsequent
367 microPET/CT imaging. PGC-1α overexpression promoted tumor growth only in the ASCL1 subtype, with
368 responses varying from a 2- to 5-fold increase in tumor volume (**Figure 5C**). To evaluate the metabolic
369 changes induced by PGC-1α overexpression in these tumors, we employed two distinct PET probes for
370 microPET/CT imaging, ^{18}F-FDG and ^{18}F-BnTP (**Figure 5A, S8B, and S8C**). ^{18}F-FDG, a glucose analog,
371 is extensively used in clinical PET imaging to measure cellular glucose uptake. While its accumulation in
372 tumors indicates increased glucose uptake, it does not provide information on the specific metabolic
373 pathways, such as whether glucose gets incorporated into the TCA cycle to fuel OXPHOS. To address
374 this limitation, we also utilized ^{18}F-BnTP, a lipophilic cation designed to accumulate specifically in the
375 mitochondrial inner membrane and measure mitochondrial membrane potential[85]. This accumulation
376 labels mitochondria with intact OXPHOS activity, offering a direct measure of mitochondrial activity and
377 content in tumors in vivo. PGC-1α overexpression enhanced uptake of both ^{18}F-BnTP (**Figure 5D**) and
378 ^{18}F-FDG (**Figure S8D**), but only in the ASCL1 subtype. However, the FDG uptake did not reach statistical
379 significance. Collectively, these findings suggest that PGC-1α overexpression promotes tumor growth in
380 the ASCL1 subtype by upregulating mitochondrial activity.

381 We next checked whether PGC-1α overexpression in tumors derived from ASCL2/POU2F3 or
382 ASCL1 cell lines resulted in increased SCN differentiation. We performed histological analysis from
383 tumors derived from both subtypes. There were no obvious histological changes in SCN differentiation
384 upon PGC-1α overexpression in either subtype (**Figure S8E**). Collectively, the data indicate that, relative
385 to the POU2F3/ASCL2 subtype, the ASCL1 subtype demonstrates dynamic metabolic plasticity,
386 exhibiting a marked OXPHOS response to PGC-1α and NDI1 overexpression. Moreover, the data
387 indicate that despite the ASCL1 subtype's greater OXPHOS response to PGC-1α overexpression, PGC-

388 1α alone is not sufficient to trigger additional neuroendocrine differentiation in these terminally
389 differentiated cell lines.
390
391 PGC-1α upregulates OXPHOS and drives SCN prostate cancer towards an ASCL1-expressing lineage.
392 We showed in Figure 5 that PGC-1α overexpression was not sufficient to induce lineage plasticity
393 of POU2F3/ASCL2 cells towards ASCL1, nor was it sufficient to induce further neuroendocrine
394 differentiation in terminally differentiated ASCL1 cells. We therefore asked whether PGC-1α
395 overexpression could promote SCN progression during PARCB transformation when the PARCB
396 oncogenes are actively restructuring the chromatin landscape to alter global gene expression. For this,
397 we conducted PARCB prostate transformation experiments with PGC-1α overexpression or control
398 constructs linked with BFP reporters, into the PARCB oncogene cocktail. (**Figure 6A**). PGC-1α
399 overexpression resulted in an approximate 100-fold increase in PGC-1α mRNA levels in PARCB prostate
400 organoids (**Figure S9A**) and a threefold higher tumor take rate compared with controls. (**Figure 6B**). The
401 majority of PGC-1α overexpressing tumors maintained high BFP expression months after transduction,
402 suggesting forward selection during transformation (**Figure S9B**). Consistently, PGC-1α protein levels
403 were higher in PGC-1α overexpressing tumors compared with control (**Figure S9C**). These data indicate
404 that PGC-1α overexpression promotes PARCB-induced SCN prostate tumor formation.
405 To better understand how PGC-1α overexpression promotes PARCB transformation, we
406 performed bulk RNA sequencing on PARCB tumors with PGC-1α overexpression and control. GSEA
407 analysis showed that gene sets related to OXPHOS were among the most significantly enriched following
408 PGC-1α overexpression in PARCB tumors (**Figure 6C**). Next, a detailed GSEA squared analysis[1]
409 (described in the methods section, and in reference[1]) was performed, ranking OXPHOS-related gene
410 sets by NES scores across multiple gene set families comprised over 10,000 gene sets (**Figure 6D**). This
411 analysis showed that OXPHOS gene sets were highly and exclusively enriched in PARCB tumors with
412 PGC-1α overexpression compared with control (**Figure 6D**). Thus, PGC-1α overexpression robustly
413 increases OXPHOS gene expression. Additionally, we explored adhesion-related pathways, known to be
414 broadly downregulated as cancers transition to a more SCN phenotype[1]. We observed a downregulation

415 of adhesion pathways in PARCB tumors that overexpressed PGC-1α, relative to the control group
416 (**Figure 6D**). These finding suggests that PGC-1α overexpression may promote SCN differentiation by
417 upregulating OXPHOS.

418 To quantify the effect of PGC-1α overexpression on SCN differentiation, we first categorized
419 tumors into PGC-1α-High and PGC-1α-Low groups, based on PGC-1α mRNA levels achieved by
420 overexpression. PGC-1α-high samples exhibited a higher SCN score compared with PGC-1α-low
421 (**Figure 6E**). We also calculated SCN scores for all 55 samples from our recently published PARCB time
422 course study[11]. Notably, PGC-1α-high samples not only displayed increased SCN differentiation in
423 comparison to the PGC-1α-low samples from this study, but also exhibited higher SCN scores than all
424 samples from the temporal study (**Figure 6E**). To determine whether these transcriptomic changes were
425 mirrored at the protein level, we performed immunohistochemistry in PARCB tumors sections with PGC-
426 1α overexpression or control. Consistent with the transcriptomic results in Figures 6C-6E, increased
427 mitochondrial content (TOMM20) and neuroendocrine (NCAM1) expression were observed in PGC-1α-
428 High tumor sections compared with PGC-1α-Low (**Figure 6F**). These results indicate that high levels of
429 PGC-1α overexpression upregulate OXPHOS expression and promote SCN differentiation.

430 Building on the established relationship between PGC-1α and ASCL1 described above, we
431 investigated if PGC-1α overexpression could promote lineage plasticity towards the ASCL1 subtype,
432 which has high neuroendocrine differentiation. By conducting a gene expression analysis on PARCB
433 tumors categorized by high versus low PGC-1α expression and analyzing signature genes of both ASCL1
434 and POU2F3/ASCL2 subtypes, we detected a distinct expression pattern. Notably, PGC-1α-high
435 samples predominantly expressed genes associated with the ASCL1 subtype, showing a 14-fold increase
436 in expression compared to PGC-1α-low samples. In contrast, PGC-1α-low samples exhibited nearly a
437 100-fold increase in the expression of POU2F3/ASCL2 subtype genes compared to PGC-1α-high
438 samples (Figure 6G). (**Figure 6G**). This pattern underscores PGC-1α's potential influence in steering
439 lineage specificity towards the ASCL1 lineage.

440 To determine if these subtype-specific expression patterns are observable in a broader clinical
441 context, our datasets from PARCB tumors with PGC-1α overexpression were projected onto datasets

442 from SCLC samples in the CCLE and from the clinical study by George et al. 2015[70] (**Figure 6H**). We
443 also included the ASCL1 and POU2F3/ASCL2 PARCB samples from our recently published study[11].
444 PGC-1α-high samples clustered well with SCLC-ASCL1 and PARCB-ASCL1 tumors (HC6), whereas
445 PGC-1α-low samples clustered better with SCLC-POU2F3 and PARCB-POU2F3/ASCL2 tumors (HC5).
446 Collectively, these data suggest that PGC-1α promotes SCNC progression towards an ASCL1-
447 expressing subtype with increased OXPHOS capacity.
448
449 **DISCUSSION**
450 PGC-1α-induced OXPHOS as a driver of lineage plasticity and progression in SCNCs
451 Metabolic reprogramming is recognized as a hallmark of many cancers, yet its direct role in driving
452 cancer progression and lineage determination remains unclear. Our findings reveal that mitochondrial
453 metabolism, driven by PGC-1α, is not only tightly correlated with SCNC subtypes but also actively drives
454 SCNC development and lineage plasticity toward the ASCL1 subtype, despite similar oncogenic stimuli
455 across subtypes. This is supported by a robust link between PGC-1α and ASCL1 in thousands of human
456 cancer cell lines and patient tumors, as well as a functional connection observed in multiple model
457 systems. These insights pave the way for further investigations into the metabolic underpinnings of
458 SCNCs, suggesting that targeted manipulation of PGC-1α or OXPHOS could offer new avenues for
459 controlling SCNC progression and differentiation.
460
461 ASCL1 as an upstream regulator of PGC-1α
462 PGC-1α is influenced by a remarkably diverse array of signals, including hormonal, nutritional,
463 and physiological stimuli, as well as potentially hundreds of transcription factors[86]. Despite its complex
464 regulatory network, PGC-1α decisively shapes specific SCNC phenotypes, effectively overriding the
465 oncogenic signals from the same set of oncogenes shared across these subtypes. This observation
466 raises an important question: what specifically regulates PGC-1α in SCNCs in a subtype-specific
467 manner? Our bioinformatics analysis, illustrated in Figure 1, along with functional experiments shown in
468 Figure 2, identify ASCL1 as a regulator of PGC-1α. Moreover, experiments depicted in Figure 6 suggest

469 that PGC-1α fosters lineage plasticity towards the ASCL1 subtype, hinting at a potential co-regulatory
470 mechanism between these two potent transcriptional regulators. While analysis of existing ASCL1 ChIP-
471 Seq datasets identified potential ASCL1 binding sites on PGC-1α promoters and gene body,
472 inconsistencies across these datasets—likely due to variations in experimental conditions and ASCL1
473 antibodies—render the evidence of direct binding inconclusive. Further research is thus necessary to
474 define the precise interaction between PGC-1α and ASCL1, including exploring indirect pathways by
475 which ASCL1 may influence PGC-1α levels.
476
477 PGC-1α and OXPHOS as metabolic vulnerabilities in SCNC subtypes
478 OXPHOS inhibition via CRISPR-mediated gene deletion, small molecule inhibitors, or PGC-1α
479 inhibition had an anti-proliferation effect in SCN cancers of both the prostate and lung. These finding
480 have clinical implications given the significant interest in targeting mitochondrial metabolism in various
481 types of cancer[46–48]. The OXPHOS inhibitor IACS-010759, targeting Complex I[46,87–89], was recently tested
482 in clinical trials. Although initial trials showing peripheral neurotoxicity and lactic acidosis[90] (on-target, off-
483 tumor toxicities), IACS-010759 demonstrated a partial response and alleviation of cancer-related pain in
484 a patient with advanced castration-resistant prostate cancer[87,91]. While recent clinical trials involving
485 IACS-010759 uncovered significant side effects, SCNCs, particularly of the POU2F3/ASCL2 subtype,
486 may offer a broader therapeutic window for OXPHOS inhibitors. These inhibitors could also be used as
487 co-therapies to enhance their efficacy in SCNCs. Targeting PGC-1α itself is another potential strategy for
488 controlling SCNC progression, with several small-molecule inhibitors that regulate PGC-1α-related
489 pathways[92]. Notably, SR-18292[81] shown to inhibit PGC-1α[93,94], reduced proliferation in SCNC-derived
490 cell lines, particularly in the POU2F3/ASCL2 subtype. While this inhibitor was reported to diminish
491 OXPHOS activity[95], its PGC-1α-related roles beyond OXPHOS in SCNCs warrant further investigation.
492 Collectively, our findings identify the PGC-1α/OXPHOS axis as a novel metabolic vulnerability in SCNCs
493 from multiple tissues.

494

495 The role of PGC-1α and OXPHOS during androgen deprivation therapy

496 Recent studies have shown that prostate cancer cells increasingly depend on OXPHOS following
497 androgen deprivation therapy (ADT)[96,97]. Our analysis of a clinical dataset, which included tumors
498 sampled from prostate cancer patients before and after ADT with enzalutamide[74], supports these
499 findings. The upregulation of PGC-1α and OXPHOS following ADT suggests that ADT imposes a
500 selection pressure on prostate cancer cells to rely more heavily on OXPHOS. This metabolic shift may
501 facilitate progression toward the SCN state. Consequently, targeting the PGC-1α-OXPHOS axis during
502 or immediately following ADT, rather than at the end-stage SCNCs, may offer an alternative therapeutic
503 approach to curb SCN prostate cancer progression.

504

505 Concluding remarks

506 Our study delineates the metabolic heterogeneity within SCNC subtypes, identifying distinct
507 metabolic profiles and capacities for OXPHOS between the ASCL1 and POU2F3/ASCL2 subtypes. We
508 demonstrate that PGC-1α not only distinguishes these subtypes but also drives metabolic
509 reprogramming, which directly alters the cancer phenotype. These findings open new avenues for
510 research and hold potential for guiding future therapies.

511

512 **MATERIALS AND METHODS**

513 ***PARCB + PGC-1α transformation***

514 Donor prostate tissues were obtained in a de-identified manner and were therefore exempt from
515 Institutional Review Board (IRB) approval. The PARCB transformation assay was performed as
516 described previously[6] with modifications to the viral constructs to include PGC-1α gain- and loss-of-
517 function analyses. Briefly, donor prostate tissues were digested overnight and isolated cells were stained
518 to identify the basal cells. FACS sorted basal cells were combined with PARCB oncogene lentiviruses at
519 an MOI of 50 in Matrigel (Cat# 356234, Corning). The mixtures of basal cells, viral supernatant, and
520 Matrigel were plated in 48-well plates as hanging drop cultures until Matrigel solidified into domes. 20,000

521 basal cells were used per Matrigel dome, in a final volume of 20-30 µl per well. After Matrigel solidification,
522 organoids were cultured in prostate organoid media[78] at 37°C and 5% CO2 for 10-14 days. Transduced
523 organoids were harvested by dissociation of Matrigel with 1mg/mL Dispase (Cat# 17105041, Thermo
524 Fisher Scientific) and washed three times with PBS to remove Dispase. Washed organoids were re-
525 suspended in 10 µl of normal Matrigel and 10 µl Matrigel with high growth factors (Cat# 354248, Corning).
526 The organoid-Matrigel mixtures were implanted subcutaneously in immunodeficient NOD.Cg-Prkdcscid
527 Il2rgtm1Wjl/SzJ (NSG) mice[79] to initiate tumor formation. Tumors were extracted before ulceration or
528 reaching around 1 cm in diameter, whichever came first. NSG mice were obtained from the Jackson
529 Laboratories and housed and bred under the care of the Division of Laboratory Animal Medicine at the
530 University of California, Los Angeles (UCLA). All animal handling and subcutaneous injections were
531 performed following the protocols approved by UCLA's Animal Research Committee.
532
533 ***Cell lines and culture media***
534 The SCN prostate cancer line NCI-H660 (Cat# CRL-5813) was purchased from American Type
535 Culture Collection (ATCC). The PARCB-P3-TP5, PARCB-P2-TP6, and PARCB-P7-TP6 cell lines[11] and
536 PARCB-1, PARCB-11[2] cell lines were generated previously. The SCN Lung Cancer Cell lines CORL-311
537 (POU2F3 subtype), NCI-H209 (ASCL1 subtype) were purchased from ATCC. LNCaP (Cat# CRL-1740)
538 and C4-2B (Cat# CRL-3315), cell lines were purchased from ATCC. SCN prostate and lung cancer cell
539 lines were maintained in stem cell culture media (SCM): Advanced DMEM/F12 (Gibco CAT# 12634028),
540 Glutamax (Gibco, CAT# 35050061), Pen/Strep, B27 (Gibco CAT# 17504044), 10ng/ml human EGF
541 (Peprotech CAT# 100-47, and 10ng/ml human FGF-basic (Peprotech CAT# 100-18B). LNCaP and C4-
542 2B cell lines were maintained in RPMI medium supplemented with 10% FBS, 100 U/mL penicillin and
543 100 µg/mL streptomycin, and 4 mmol/L GlutaMAX. All cell lines were routinely tested for Mycoplasma
544 using a MycoAlert™ PLUS Mycoplasma Detection Kit (Cat# LT07-703, Lonza).
545

546 ***Lentiviral vectors and high-titer lentivirus production***

547 The following three vectors for PARCB transformation were described previously: mristoylated
548 AKT1 (FU-myrAKT1-CGW), c-MYC and BCL2 (FU-cMYC-P2A-BCL2-CRW), dominant negative TP53
549 (R175H) and shRNA targeting of RB1 (FU-shRB1-TP53DN-CYW)[6]. For PGC-1α overexpression, a fourth
550 vector was designed. First, an FUGW backbone was subcloned to replace the EGFP with EBFP2 using
551 Gibson assembly (referred to as FUBW). Next, PGC-1α cDNA from pcDNA4 myc PGC-1 alpha (Addgene
552 #10974) was cloned into the FUBW backbone driven by a ubiquitin promoter. An empty FUBW backbone
553 without PGC-1α cDNA was used as a control. For PGC-1α inhibition during PARCB transformation,
554 shRNA targeting PGC-1α was cloned into the myristoylated AKT1 vector (FU-myrAKT1-CGW),
555 downstream of the H1 promoter. The following PGC-1α targeting sequence was used
556 TATGACAGCTACGAGGAATAT. As a control, a sequence that targets no known mammalian genes was
557 used (CAACAAGATGAAGAGCACCAA). For PGC-1α inhibition in cultured cell lines, the same shRNA
558 sequences were cloned into a pLKO_005 backbone, which was subcloned to replace its puromycin
559 resistance gene along with its promoter with CMV-EBFP2. High titer lentiviruses were made using a
560 previously established method[162].

561

562 ***Transduction of cultured SCN cell lines***

563 Cultured SCN cell lines, which grow in suspension as clusters, were mechanically dissociated
564 using gentle pipetting with a P1000 pipette. 600,000 live cells were seeded in non tissue culture treated
565 12-well plates and transduced with high titer lentiviruses at an MOI of 2-5 in the presence of polybrene
566 and ROCK inhibitor. The plates were subsequently centrifuged at 1,000 g for 90 min at RT, followed by
567 overnight incubation. The following morning, 1 ml fresh SCM was added to each well and the cells were
568 gently mixed with a P1000 to dislodge any adhered cells. 48-72 hours after transduction, BFP positive
569 cells were sorted to enrich for transduced cells. After a 24-hour recovery period, cells were used for
570 downstream analyses.

571

572 ***PRNBSA-induced SCN prostate cancer transdifferentiation in vitro***

573 PNRBSA transduction experiments were performed as described previously[77]. Cells were seeded
574 in 6-well tissue culture plates at a density of 3 x 105 cells per mL in 3 mL of RPMI medium supplemented
575 with 10% FBS, 100 U/mL penicillin and 100 µg/mL streptomycin, and 4 mmol/L GlutaMAX. Cells were
576 transduced approximately 4-6 hours after seeding at a defined multiplicity of infection (MOI) of 4 for each
577 lentivirus. 72 hours after transduction, cells were trypsinized, washed, and transferred to 100 mm tissue
578 culture plates in 15 mL of neural stem cell media (N-SCM) consisting of Advanced DMEM/F12 medium
579 supplemented with 1X serum-free B27, 10 ng/mL recombinant human bFGF, 10 ng/mL recombinant
580 human EGF, 100 U/mL penicillin and 100 µg/mL streptomycin, and 4 mmol/L GlutaMAX. Media were
581 replenished every 3-4 days. Cells were collected 14 days post-transduction for analysis.

582

583 ***Cell proliferation assay***

584 2,000 - 10,000 cells per cell line in 3-6 replicates were seeded into black, opaque 96-well plates
585 with a glass bottom. Cell content was measured on Days 1-6 using Cell Titer-Glo Luminescent Cell
586 Viability Assay (Cat# G7570, Promega). Luminescence was measured at an integration time of 0.5
587 second per well. The number of cell doublings were calculated between the day of plating, and the
588 termination of the assay, indicated on each figure panel. Because CTG uses an ATP-based readout, and
589 since the mitochondrial inhibitors influence the amount of ATP in the cell, the internal GFP, driven by the
590 AKT1 (FU-myrAKT1-CGW) vector was also quantified using microscopy and a plate reader. Consistent
591 results were obtained with both techniques.

592

593 ***Inhibition of PGC-1α and OXPHOS***

594 For pharmacological inhibition of PGC-1α (with SR-18292) and OXPHOS (with IACS-010759 and
595 IMT1B), 96-well plates were pre-filled with SCM media (described above) containing each of the inhibitors
596 or DMSO as a control. Cell growth was quantified using the Cell Titer-Glo Luminescent Cell Viability
597 Assay (Cat# G7570, Promega) as described below.

598

599 ***RT-qPCR***

600 Total RNA was isolated from cells using miRNeasy Mini Kit (Cat# 217004, Qiagen). cDNA was
601 synthesized from 2 ug of total RNA using the SuperScript IV First-Strand Synthesis System (Cat#
602 18091050, Thermo Fisher). RT-qPCR was performed using SYBR Green PCR Master Mix (Cat#
603 4309155, Thermo Fisher). Amplification was carried out using the StepOne Real-Time PCR System
604 (Cat# 4376357, Thermo Fisher) and analysis was performed using the StepOne Software v2.3. Relative
605 quantification was determined using the Delta-Delta Ct Method. The following primer pair was used to
606 amplify PGC-1α mRNA:

607 CCTGCTCGGAGCTTCTCAAA

608 CCCTTGGGGTCATTTGGTGA

609

610 ***Tissue section, histology, and immunohistochemistry (IHC)***

611 PARCB tumors were fixed by overnight nutation in 10% buffered formaldehyde (SF100-4) at 4℃
612 followed by three washes in 70% ethanol. Hematoxylin and eosin (H&E) staining was performed by
613 UCLA's Translation Pathology Core Laboratory (TPCL) using standard protocols. TPCL is a CAP/CLIA
614 certified research facility in the UCLA Department of Pathology and Laboratory Medicine and a UCLA
615 Jonsson Comprehensive Cancer Center Shared Facility. For immunohistochemistry, formalin-fixed,
616 paraffin-embedded (FFPE) PARCB tumors were deparaffinized in xylene and rehydrated. Citrate buffer
617 (pH=6.0) was used for antigen retrieval. The sections were incubated in citrate buffer and heated in a
618 pressure cooker. 3% H2O2 in methanol was used to block endogenous peroxidase activity for 10 min at
619 room temperature. The sections were blocked then incubated with primary antibodies overnight at 4°C.
620 Anti-mouse/rabbit secondary antibodies were used to detect proteins of interest and DAB EqV substrate
621 was used to visualize the staining. All components were included in the ImmPRESS Kit (MP-7801-15
622 and MP-7802-15, Vector Laboratories). The slides were then dehydrated and mounted with Xylene-
623 based drying medium (Cat# 22-050-262, Fisher Scientific).

624

625 ***Western blot***

626 1 million viable cells were lysed on ice using RIPA lysis buffer (Cat#89900, Thermo Fisher).
627 Protein concentrations were measured using the Pierce BCA Protein Assay Kit (Cat#: 23227, Thermo
628 Scientific). Samples were electrophoresed on polyacrylamide gels (Cat# NW04120BOX, Thermo Fisher),
629 transferred to PVDF membranes (Cat# IPVH00010, Millipore). Western blots were visualized using
630 iBright CL1500 Imaging system (Cat#44114, Thermo Fisher).

631

632 ***Antibodies***

633 The following antibodies were used: PGC-1α ms monoclonal 4C1.3 (Sigma, ST1202), TOMM20
634 ms monoclonal (Santa Cruz Biotechnology, sc-17764), NCAM1/CD56 (Abcam, ab133345), and
635 OXPHOS cocktail ms monoclonal (Abcam, ab110411).

636

637 ***Bulk RNA sequencing and dataset collection***

638 Tumors were dissociated into single cells, followed by cell sorting of quadruple colors (BFP, GFP,
639 YFP, and RFP) by flow cytometry. Total RNA was extracted from the cell lysates using the Zymo Direct-
640 zol RNA Miniprep Plus Kit (Cat. No: R2072). Quality check was performed on the Agilent 4200
641 Tapestation (Agilent Technology; cat. no. G2991BA). Libraries for RNA-Seq of PARCB with PGC-1α
642 overexpression and control samples were prepared with KAPA Stranded mRNA-Seq Kit (Cat# KK8420,
643 Roche). The workflow consists of mRNA enrichment and fragmentation. Sequencing was performed on
644 Illumina Hiseq 3000 or NovaSeq 6000 for PE 2x150 run. Data quality check was done on Illumina SAV.
645 Demultiplexing was performed with Illumina Bcl2fastq v2.19.1.403 software. Raw sequencing reads were
646 processed through the UCSC TOIL RNA Sequencing pipeline for quality control, adapter trimming,
647 sequence alignment, and expression quantification. Briefly, sequence adapters were trimmed using
648 CutAdapt v1.9, sequences were then aligned to human reference genome GRCh38 using STAR v2.4.2a
649 and gene expression quantification was performed using RSEM v1.2.25 with transcript annotations from
650 GENCODE v23[83].

651 The FASTQ files of the Park dataset[6], Beltran dataset[33], George dataset[32], Rajan dataset[124]
652 (GSE48403), and Chen dataset were all processed through the TOIL pipeline with the same parameters
653 to get RSEM expected counts. The TOIL-RSEM expected counts of TCGA pan cancer samples were
654 obtained directly from UCSC Xena browser (https://xenabrowser.net/datapages) and RSEM read counts
655 of pan-cancer cell lines from the Cancer Cell Line Encyclopedia (CCLE) were downloaded from DepMap
656 Portal (DepMap Public 22Q1) (https://depmap.org/portal/download/all/). The RSEM counts of all
657 combined datasets were upper quartile normalized with a pseudocount of 1 and log2 transformed
658 (referred to as log2 (UQN+1) counts) and filtered down to HUGO protein coding genes
659 (http://www.genenames.org/) for the downstream analyses. SCLC subtypes[43] and CRPC subtypes[54]
660 were previously defined.

661 Sequencing of high-grade serous ovarian carcinomas (HGSOC) was approved through UCLA
662 Institutional Review Board (IRB) approved protocols (IRB #10-000727, IRB #20-001626). Tumor
663 specimens were obtained from high-grade serous ovarian cancer patients who had given their informed
664 consent. RNA was isolated from both solid tumors collected from primary and metastatic sites, and
665 effusion samples such as ascites and pleural fluid. Dissociated or cryopreserved tumor fragments were
666 used for isolation of RNA. These samples were collected at various disease time points: chemonaive,
667 post adjuvant or neoadjuvant chemotherapy, and at disease recurrence. Presence of tumor cells was
668 confirmed on histologic sections. RNA isolation, library preparation, and sequencing were conducted by
669 the Technology Center for Genomics and Bioinformatics (TCGB) core facility at UCLA.

670

671 ***Differential gene expression analysis and hierarchical clustering***

672 Differential expression analysis was performed on raw RSEM expected count data of protein-
673 coding genes using the R package DESeq2[98].

674

675 ***Gene set enrichment analysis (GSEA) and GSEA-squared***

676 Differential gene expression analysis was first performed on raw RSEM expected count data of
677 protein-coding genes on the Rajan 2014[124] dataset between Pre-ADT and Post-ADT samples.

678 Using the fgsea R package (https://github.com/ctlab/fgsea), gene set enrichment analysis (GSEA) was
679 then performed on the hallmark (H), canonical pathways (CP), and gene ontology (GO) gene sets from
680 MSigDB[99]. Additional mitochondria related gene sets were also included from MitoCarta3.0. The ranked
681 list of genes was generated using the signed log2 fold change and -log10 transformed p-values calculated
682 by DESeq2[100]. GSEA results were then ranked by Normalized Enrichment Score (NES) to identify highly
683 enriched gene sets. To investigate pathways broadly related to our highly enriched gene sets (e.g.,
684 oxidative phosphorylation and adhesion), GSEA-Squared analysis was performed. In short, gene sets
685 were ranked by NES and marked for if they contained a key term from that category of terms in the
686 pathway name. KS tests were then performed using ks.test.2 to assess the distribution of the category
687 of terms[100]. The keys used were the following:
688
689 Oxidative Phosphorylation, OXIDATIVE PHOSPHORYLATION, ELECTRON TRANSPORT,
690 MITOCHONDRIAL COMPLEX, NADH DEHYDROGENASE, MITOCHONDRIAL LARGE RIBOSOMAL;
691 OXPHOS
692 Adhesion, ADHESION, ADHERENS
693
694 Differential gene expression analysis was also performed on raw RSEM expected count data of
695 protein-coding genes on the Chen 2014[32] dataset between HC6/ Class II/ ASCL1+ tumors and the rest
696 of the samples in the dataset. Similar methods were used to perform gene set enrichment analysis on
697 GO BP 2021 gene sets from MSigDB, except genes were ranked by their adjusted p-value.
698
699 ***Principle component analyses***
700 Unsupervised principal component analysis (PCA) was performed on log2 transformed upper
701 quartile normalized RSEM expected count data. The prcomp function in R was run centered and
702 unscaled. Data was projected onto the PCA framework by multiplying the rotation matrix by the projected
703 data's expression matrix.
704

705 ***Small cell neuroendocrine (SCN) score***

706 SCN score was calculated as previously described in Balanis et al[1]. Briefly, PC1 loadings were
707 taken from a pan-cancer PCA which followed non-small cell cancers along their transdifferentiation
708 trajectory towards an SCN phenotype. A higher SCN score indicates a more SCN-like phenotype, while
709 a lower SCN score indicates a more normal, non-SCN-like phenotype.

710

711 ***Motif analysis***

712 ATAC sequencing data was obtained from Chen 2023 dataset[32]. The raw FASTQ files were
713 processed using the published ENCODE ATAC-Seq Pipeline (https://github.com/ENCODE-
714 DCC/atacseq-pipeline). The reads were trimmed and aligned to hg38 using bowtie2. Picard was used to
715 de-duplicate reads, which were then filtered for high-quality paired reads using SAMtools. All peak calling
716 was performed using MACS3. The optimal irreproducible discovery rate (IDR) thresholded peak output
717 was used for all downstream analyses, with a threshold P value of 0.05. Other ENCODE3 parameters
718 were enforced with the flag-encode3. Reads that mapped to mitochondrial genes or blacklisted regions,
719 as defined by the ENCODE pipeline, were removed. The peak files were merged using bedtools merge
720 to create a consensus set of peaks across all samples, and the number of reads in each peak was
721 determined using bedtools multicov[101]. A variance stabilizing transformation was performed on peak
722 counts using DESeq2[98] and batch effects were removed using removeBatchEffect from limma[102].
723 DESeq2 was then used to variance stabilize transform read counts and determine hyper- and hypo-
724 accessible peaks across HC5 and HC6 PARCB time course samples, using default parameters and
725 without independent filtering or Cook's cutoff. Peaks were called as hyper or hypo-accessible using
726 abs(log2 fold change)>2 and adjusted p<0.05. Motif analysis was then run separately on hyper- or hypo-
727 accessible peaks in the HC5 versus. HC6 comparison using HOMER[103] with the flags -size 200 and -
728 mask. Motifs were then ranked by their p-value for hyper- or hypo-accessible peak sets. Motifs specific
729 to hyper or hypo accessible peaks were obtained by taking the rank difference of the motifs in the two
730 lists.

731

732 ***Single-cell RNA sequencing analyses***

733 Single-cell expression levels of ASCL1, PGC-1α, ASCL2, and POU2F3 in PARCB time course
734 tumors were extracted from our recently published study[11]. Gene expression was visualized using
735 Uniform Manifold Approximation and Projection (UMAP) analysis as described previously[11]. The
736 downstream quality control, as well as batch integration and correction of PARCB single cell RNA-seq
737 data were performed as described previously[11]. Briefly, visualization of PARCB single cell RNA-seq data
738 was performed using the Seurat (5.0.3) R package[104]. The top 30 principal components were used to
739 perform UMAP analysis. Cell clustering was performed with FindNeighbors function with top 30 principal
740 components and FindClusters function with resolution of 0.5.

741

742 ***Seahorse respirometry***

743 Respirometry experiments were performed on a Seahorse XF96 Extracellular Flux Analyzer
744 (Agilent Technologies). PARCB tumor-derived cell lines were process and counted as described, washed
745 into Seahorse Assay medium (Seahorse XF Base Medium supplemented with 2 mM L-glutamine, 1 mM
746 pyruvate and 10 mM glucose) and immediately seeded into an XF96 microplate, pre-coated with PDL.
747 Cells were plated at a density of 40,000 cells per well in a final volume of 175 µl. Prior to the start of the
748 assay, the XF96 plate was placed in a 37 °C incubator without CO2 for 30 min. During the assay, the
749 following compounds were injected: the mitochondrial ATP synthase inhibitor oligomycin (final
750 concentration 2 µM); the mitochondrial uncoupler FCCP (final concentration 1 µM); and the complex I
751 and III inhibitors rotenone (final concentration 2 µM); and the complex III inhibitor antimycin A (final
752 concentration 2 µM). At the conclusion of the assay, the cells were fixed with 4% paraformaldehyde,
753 stained with Hoechst, and cell number per well was determine based on nuclei number using an Operetta
754 High-Content Imaging System (PerkinElmer). OCRs were normalized to cell number per well.

755

756 ***microPET/CT imaging of tumor metabolism***

757 Tumor-bearing mice were injected with 60 µCi of [^{18}F]-FDG (PETNET Solutions) or [^{18}F]-BnTP
758 (prepared as previously described[105] through tail vein intravenous injections. Following a 60-minute

759 unconscious uptake of the imaging tracer, mice were anesthetized with 2% vaporized isoflurane, and
760 microPET (energy window 350-650 keV, 10-min static scan) and microCT (voltage 80 kVp, current 150
761 μA, 720 projections, 200μm resolution, scan time 1 min) images were acquired on a GNEXT PET/CT
762 scanner (Sofie Biosciences, Dulles, VA). The microPET images were reconstructed using a 3D-Ordered
763 Subset Expectation Maximization (OSEM) algorithm (24 subsets and 3 iterations), with random,
764 attenuation, and decay correction. The microCT images were reconstructed using a Modified Feldkamp
765 Algorithm. Amide software was used to analyze co-registered microPET/CT images. Representative
766 maximum-intensity-projection (MIP) images are shown.
767
768 ***Chromatin immunoprocepticiation sequencing (ChIP-Seq)***
769 To analyze the regulatory impact of ASCL1 on PGC-1α, we utilized Chromatin
770 Immunoprecipitation Sequencing (ChIP-Seq) and CUT&RUN data from several studies, including
771 Augustyn et al., 2014 (GSE61197), Borromeo et al., 2016 (GSE69398), Cejas et al., 2021 (GSE156290),
772 and Nouruzi et al., 2022 (GSE183198), which were downloaded directly from the Gene Expression
773 Omnibus (GEO). We converted data from bedGraph and wig formats to bigWig format using the UCSC
774 bedGraphToBigWig and wigToBigWig tools to standardize data representation. To align all datasets to a
775 consistent reference genome, we lifted data initially mapped to hg19 over to hg38 using the UCSC liftOver
776 tool. For the Li et al., 2024 ChIP-Seq dataset[77], we merged bigWig files from replicates at each timepoint
777 using the UCSC bigWigMerge tool, aiming to consolidate data for comprehensive analysis. Visualization
778 of the processed datasets was performed with the Integrative Genomics Viewer (IGV 2.17.1), ensuring
779 uniform background noise levels across samples to facilitate accurate comparison.

MAIN FIGURES AND LEGENDS

Figure 1

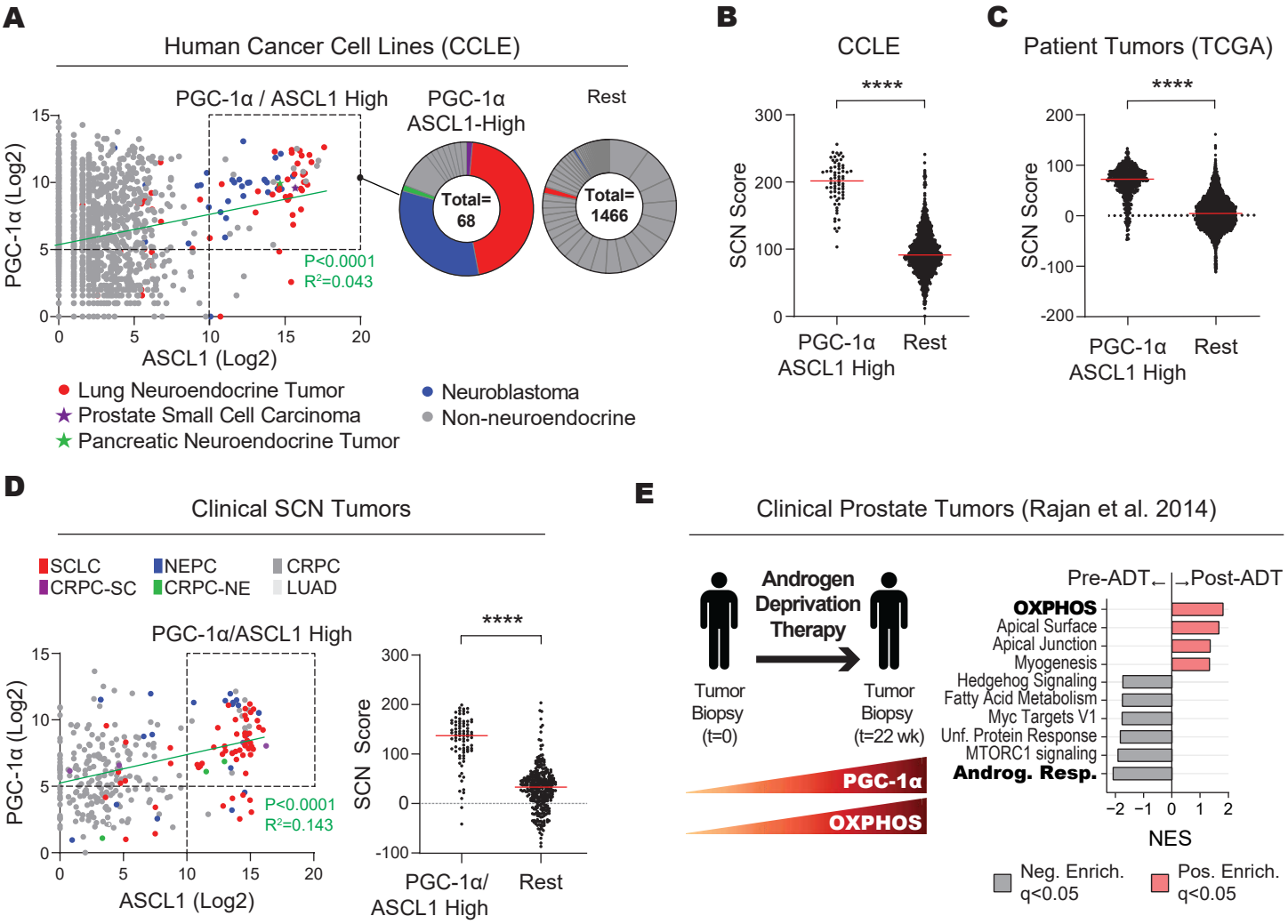

780 **Figure 1.** Elevated PGC-1α in clinical SCNC correlates with increased ASCL1 expression and
781 neuroendocrine differentiation.

782 A. Gene expression analysis across all human cancer cell lines from the Cancer Cell Line
783 Encyclopedia (CCLE). Left panel: co-expression analysis between PGC-1α and ASCL1,
784 highlighting samples with high expression levels of both genes (boxed region). Right panel: pie
785 charts illustrating the proportion of cancer types exhibiting elevated co-expression of PGC-1α and
786 ASCL1, in contrast to the rest of the samples. See also Figure S1A.

787 B. Related to Figure 1A and S1B: Transcriptomic examination of small cell neuroendocrine (SCN)
788 differentiation in CCLE human cancer cell lines. SCN scores (defined previously[3] and detailed in
789 the Methods) are calculated for cells showing heightened PGC-1α and ASCL1 expression versus
790 the rest of the cells.

791 C. Related to Figure S1C: A transcriptomic analysis of SCN differentiation in all the patient tumors
792 from the TCGA database shown in Figure S1C. SCN scores are calculated from the boxed tumor
793 samples with elevated PGC-1α and ASCL1 expression compared with the rest of the samples.

794 D. Gene expression analysis in multiple clinical SCNC datasets[66–70,106]. Left panel: co-expression
795 analysis of PGC-1α and ASCL1. Right panel: SCN scores of the boxed samples with elevated
796 PGC-1α and ASCL1 expression compared with the rest of the samples.

797 E. Transcriptomic analyses in clinical prostate cancer tumors before and after androgen deprivation
798 therapy (ADT) with enzalutamide. Left panel: a schematic overview. Right panel: gene set
799 enrichment analysis (GSEA) of differentially expressed genes in pre- versus post ADT-treated
800 tumors. See also Figure S1F.

801

802 Data for Figures 1B-1D are expressed as mean ± SEM, with significance denoted as **** ($p \leq 0.0001$),
803 ** ($p \leq 0.01$), and * ($p \leq 0.05$). The green lines represent the best-fit linear regression model, with the
804 indicated R^2 and p-values. All Log2 values have been upper quartile normalized with a pseudocount
805 of 1 (Log2 UQN+1). For statistical tests used, see Material and Methods section.

806 Related data can be found in Figure S1. Abbreviations: SCLC, small cell lung cancer; NEPC,
807 neuroendocrine prostate cancer; CRPC, castration resistant prostate cancer; LUAD, lung
808 adenocarcinoma.

Figure 2

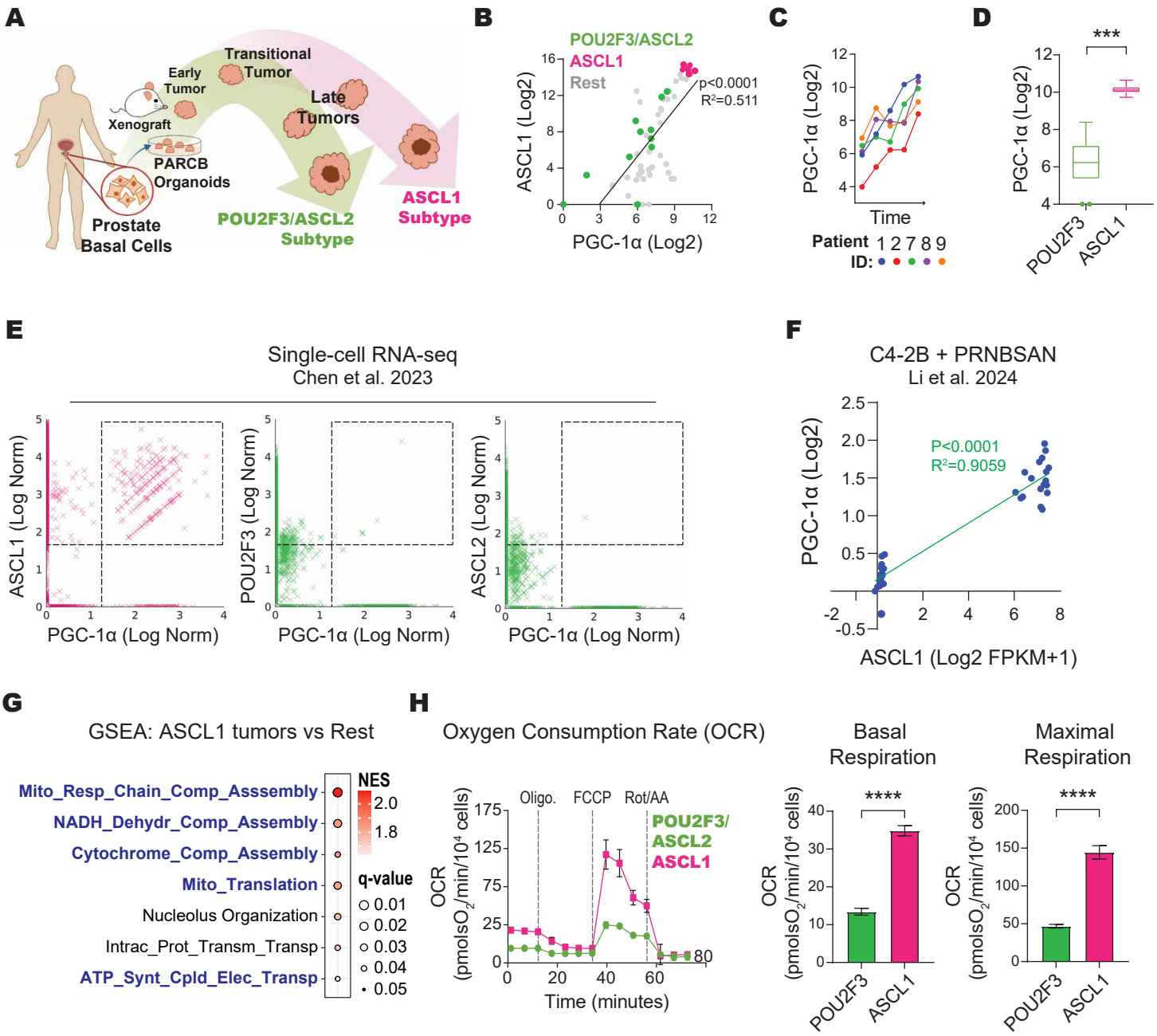
A
Transitional Tumor
Early Tumor
Xenograft
Late Tumors
PARCB Organoids
Prostate Basal Cells
POU2F3/ASCL2 Subtype
ASCL1 Subtype
B
POU2F3/ASCL2
ASCL1
Rest
p<0.0001
R²=0.511
ASCL1 (Log2)
PGC-1α (Log2)
C
PGC-1α (Log2)
Time
Patient ID: 1 2 7 8 9
D
***
PGC-1α (Log2)
POU2F3
ASCL1
E
Single-cell RNA-seq
Chen et al. 2023
ASCL1 (Log Norm)
POU2F3 (Log Norm)
ASCL2 (Log Norm)
PGC-1α (Log Norm)
F
C4-2B + PRNBSAN
Li et al. 2024
P<0.0001
R²=0.9059
PGC-1α (Log2)
ASCL1 (Log2 FPKM+1)
G
GSEA: ASCL1 tumors vs Rest
Mito_Resp_Chain_Comp_Asssembly
NADH_Dehydr_Comp_Assembly
Cytochrome_Comp_Assembly
Mito_Translation
Nucleolus Organization
Intrac_Prot_Transm_Transp
ATP_Synt_Cpld_Elec_Transp
NES
2.0
1.8
q-value
0.01
0.02
0.03
0.04
0.05
H
Oxygen Consumption Rate (OCR)
Oligo.
FCCP
Rot/AA
POU2F3/
ASCL2
ASCL1
OCR (pmolsO2/min/10⁴ cells)
Time (minutes)
Basal Respiration
Maximal Respiration
****
POU2F3
ASCL1

809 **Figure 2.** Enhanced PGC-1α expression and OXPHOS activity in SCN prostate cancer within the ASCL1
810 tumor subtype.

811 A. Schematic illustrating PARCB-induced SCN prostate transformation, highlighting the bifurcation
812 of end stage tumors into the POU2F3/ASCL2 and ASCL1 lineages. The schematic is modified
813 from Chen et al. 2023[11].

814 B. Co-expression analysis of PGC-1α and ASCL1 during PARCB prostate transformation. Note that
815 tumors with the highest expression levels of both genes are exclusively found in the ASCL1
816 subtype. The black line represents the best-fit linear regression model, with the indicated R^2 and
817 p-values.

818 C. Analysis of PGC-1α expression levels during PARCB transformation in 5 out of 10 patient series
819 showcasing increased PGC-1α expression over time.

820 D. Comparative expression levels of PGC-1α in POU2F3/ASCL2 versus ASCL1 PARCB tumor
821 subtypes indicating increased PGC-1α expression in the ASCL1 subtype.

822 E. Single cell gene expression levels of PGC-1α vs ASCL1, POU2F3, and ASCL2 from the PARCB
823 time course tumors from Chen et al. 2023[11].

824 F. Co-expression analysis of PGC-1α and ASCL1 in C4-2B cells from the PRNBSAN transformation
825 system[77]. Log2 values are Log2 FPKM+1.

826 G. GSEA in the ASCL1 tumor subtype versus the rest of the PARCB time course samples. Gene
827 Ontology Biological Process (GOBP) gene sets were used. The pie chart indicates the proportion
828 of enriched gene sets related to mitochondrial OXPHOS.

829 H. Seahorse respirometry in PARCB tumor-derived cell lines from both the POU2F3/ASCL2 and
830 ASCL1 subtypes. Inhibitors used: Oligo, Oligomycin; FCCP, Carbonyl cyanide-p-
831 trifluoromethoxy-phenylhydrazone; Rot/AA, rotenone / antimycin A.

832

833 All data, except in Figure 2F, utilizes data extracted from our recently published Chen et al. 2023
834 dataset[11]. Data in Figures 2D, 2F, and 2H are presented as mean ± SEM, with significance levels

835 marked as follows: **** ($p \leq 0.0001$), *** ($p \leq 0.001$), ** ($p \leq 0.01$), and * ($p \leq 0.05$). All Log2 values are

836 Log2 UQN+1 unless otherwise noted. For statistical tests used, see Material and Methods section.

837

838 Related data can be found in Figure S2-S6.

Figure 3

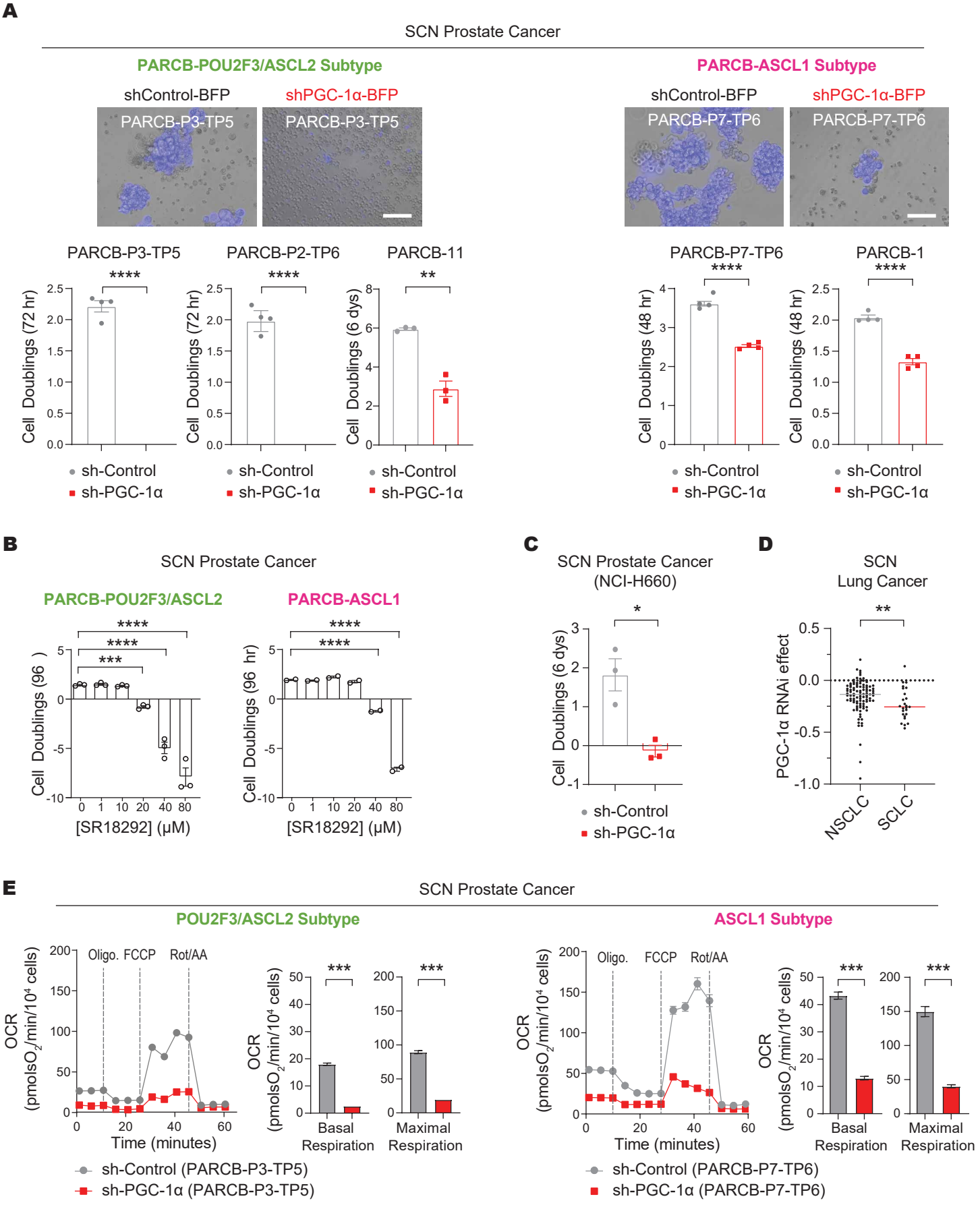
A
SCN Prostate Cancer
PARCB-POU2F3/ASCL2 Subtype
PARCB-ASCL1 Subtype
shControl-BFP
shPGC-1α-BFP
PARCB-P3-TP5
PARCB-P7-TP6
PARCB-P2-TP6
PARCB-11
PARCB-1
Cell Doublings (72 hr)
Cell Doublings (6 dys)
Cell Doublings (48 hr)
sh-Control
sh-PGC-1α
B
SCN Prostate Cancer
PARCB-POU2F3/ASCL2
PARCB-ASCL1
Cell Doublings (96)
Cell Doublings (96 hr)
[SR18292] (μM)
C
SCN Prostate Cancer
(NCI-H660)
Cell Doublings (6 dys)
D
SCN
Lung Cancer
PGC-1α RNAi effect
NSCLC
SCLC
E
SCN Prostate Cancer
POU2F3/ASCL2 Subtype
ASCL1 Subtype
Oligo.
FCCP
Rot/AA
OCR (pmolsO2/min/10^4 cells)
Time (minutes)
Basal Respiration
Maximal Respiration
sh-Control (PARCB-P3-TP5)
sh-PGC-1α (PARCB-P3-TP5)
sh-Control (PARCB-P7-TP6)
sh-PGC-1α (PARCB-P7-TP6)

839 **Figure 3.** PGC-1α inhibition blunts OXPHOS, reduces the growth of SCNC cell lines, and blocks SCN
840 prostate tumor formation.

841 A. Cell proliferation analysis in PARCB tumor-derived cell lines comparing PGC-1α knockdown (KD)
842 cells to control. The blue fluorescence in the micrographs is derived from the shPGC-1α and
843 shControl constructs, which have co-linked expression of a blue florescence protein (see methods
844 section for details).

845 B. Cell proliferation analysis of PARCB tumor-derived cell lines treated with SR-18292, a
846 pharmacological inhibitor of PGC-1α.

847 C. Cell proliferation analysis of a patient-derived SCN prostate cancer cell line (NCI-H660) with PGC-
848 1α KD compared with control.

849 D. PGC-1α inhibition (RNAi) effects on cell proliferation, represented by a dependency scores from
850 the DepMap database. A score of zero signifies no proliferation impact, negative values indicate
851 decreased proliferation, and a score of negative one corresponds to the median effect across all
852 pan-essential genes.

853 E. Seahorse respirometry in PARCB cell lines derived from the POU2F3/ASCL2 and ASCL1 tumor
854 subtypes. Oligo, Oligomycin; FCCP, Carbonyl cyanide-p-trifluoromethoxy-phenylhydrazone;
855 Rot/AA, rotenone / antimycin A.

856

857 All data are presented as mean ± SEM, with significance levels marked as follows: *** ($p \leq 0.001$), **
858 ($p \leq 0.01$), and * ($p \leq 0.05$). For statistical tests used, see Material and Methods section.

859

860 Related data can be found in Figure S7.

Figure 4

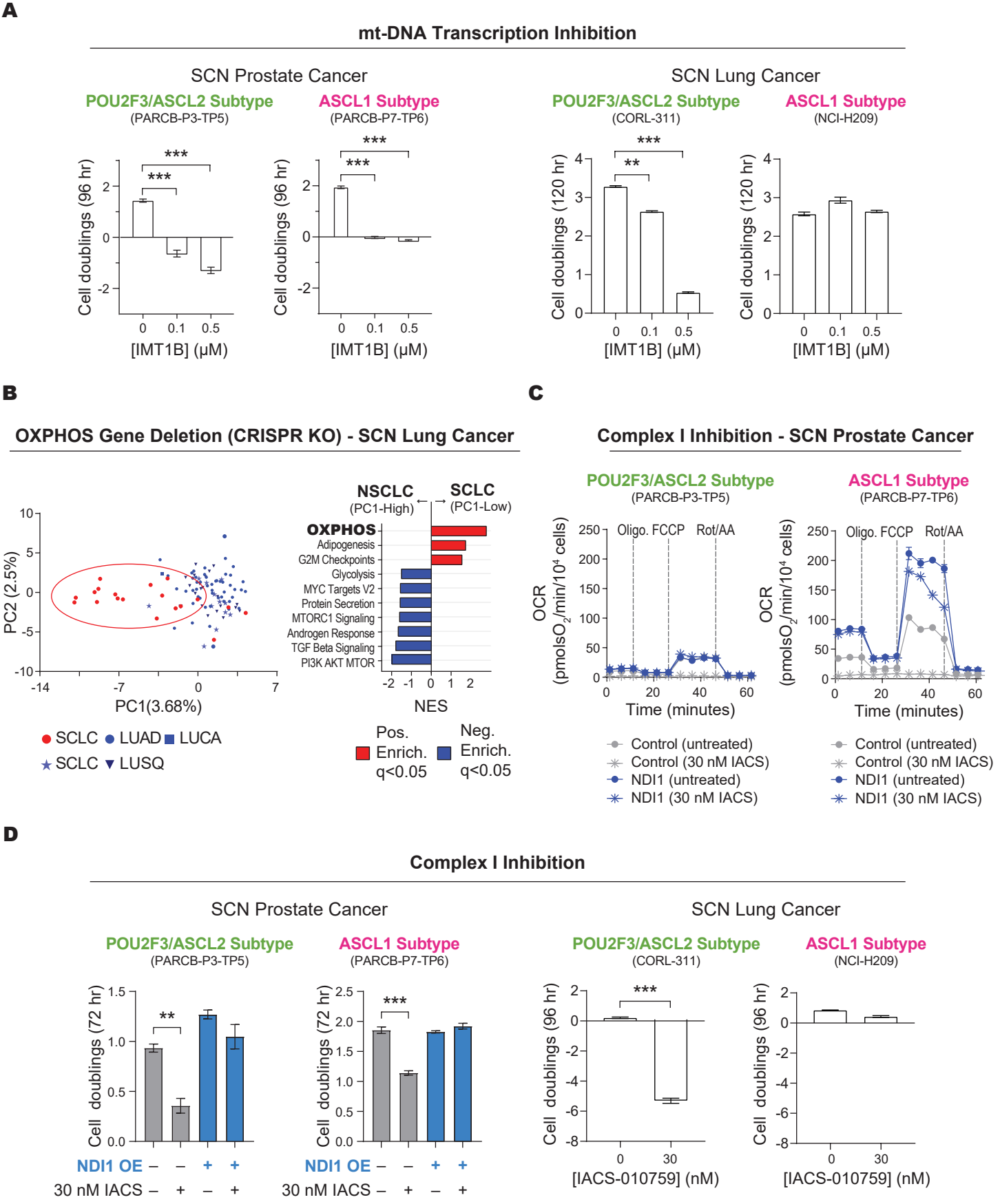
A
mt-DNA Transcription Inhibition
SCN Prostate Cancer
POU2F3/ASCL2 Subtype
(PARCB-P3-TP5)
ASCL1 Subtype
(PARCB-P7-TP6)
SCN Lung Cancer
POU2F3/ASCL2 Subtype
(CORL-311)
ASCL1 Subtype
(NCI-H209)
Cell doublings (96 hr)
Cell doublings (120 hr)
[IMT1B] (μM)
B
OXPHOS Gene Deletion (CRISPR KO) - SCN Lung Cancer
PC2 (2.5%)
PC1(3.68%)
SCLC
LUAD
LUCA
SCLC
LUSQ
NSCLC
(PC1-High)
SCLC
(PC1-Low)
OXPHOS
Adipogenesis
G2M Checkpoints
Glycolysis
MYC Targets V2
Protein Secretion
MTORC1 Signaling
Androgen Response
TGF Beta Signaling
PI3K AKT MTOR
NES
Pos. Enrich. q<0.05
Neg. Enrich. q<0.05
C
Complex I Inhibition - SCN Prostate Cancer
POU2F3/ASCL2 Subtype
(PARCB-P3-TP5)
ASCL1 Subtype
(PARCB-P7-TP6)
OCR (pmolsO2/min/10⁴ cells)
Oligo.
FCCP
Rot/AA
Time (minutes)
Control (untreated)
Control (30 nM IACS)
NDI1 (untreated)
NDI1 (30 nM IACS)
D
Complex I Inhibition
SCN Prostate Cancer
POU2F3/ASCL2 Subtype
(PARCB-P3-TP5)
ASCL1 Subtype
(PARCB-P7-TP6)
SCN Lung Cancer
POU2F3/ASCL2 Subtype
(CORL-311)
ASCL1 Subtype
(NCI-H209)
Cell doublings (72 hr)
Cell doublings (96 hr)
NDI1 OE
30 nM IACS
[IACS-010759] (nM)

861 **Figure 4.** OXPHOS inhibition blunts SCN prostate and lung cancer cell line proliferation.

862 A. Cell proliferation analysis of cell lines derived from the SCN prostate and lung cancer
863 POU2F3/ASCL2 and ASCL1 tumor subtypes treated with IMT1B, a mitochondrial DNA-directed
864 RNA polymerase (POLRMT) inhibitor to block OXPHOS.

865 B. Analysis of differentially dependent genes in NSCLC and SCLC cell lines. Left panel:
866 unsupervised principal component analysis (PCA) on the genetic dependency data from all of the
867 lung cancer cell lines in the DepMap dataset. Right panel: normalized enrichment scores of gene
868 sets that separate PC1 low (SCLC) and PC1 high (NSCLC). The top 100 genes from the PC1
869 loading scores were used as input.

870 C. Seahorse respirometry in cell lines derived from the PARCB POU2F3/ASCL2 and -ASCL1 tumor
871 subtypes with the indicated conditions. Oligo, Oligomycin; FCCP, Carbonyl cyanide-p-
872 trifluoromethoxy-phenylhydrazone; Rot/AA, rotenone / antimycin A.

873 D. Cell proliferation analysis of cell lines derived from the SCN prostate and lung cancer
874 POU2F3/ASCL2 and ASCL1 subtypes with the indicated treatments.

875

876 Data in Figure 4B are represented as mean ± SEM. with statistical significance denoted as ***
877 ($p \leq 0.001$) and ** ($p \leq 0.01$). For statistical tests used, see Material and Methods section.

Figure 5

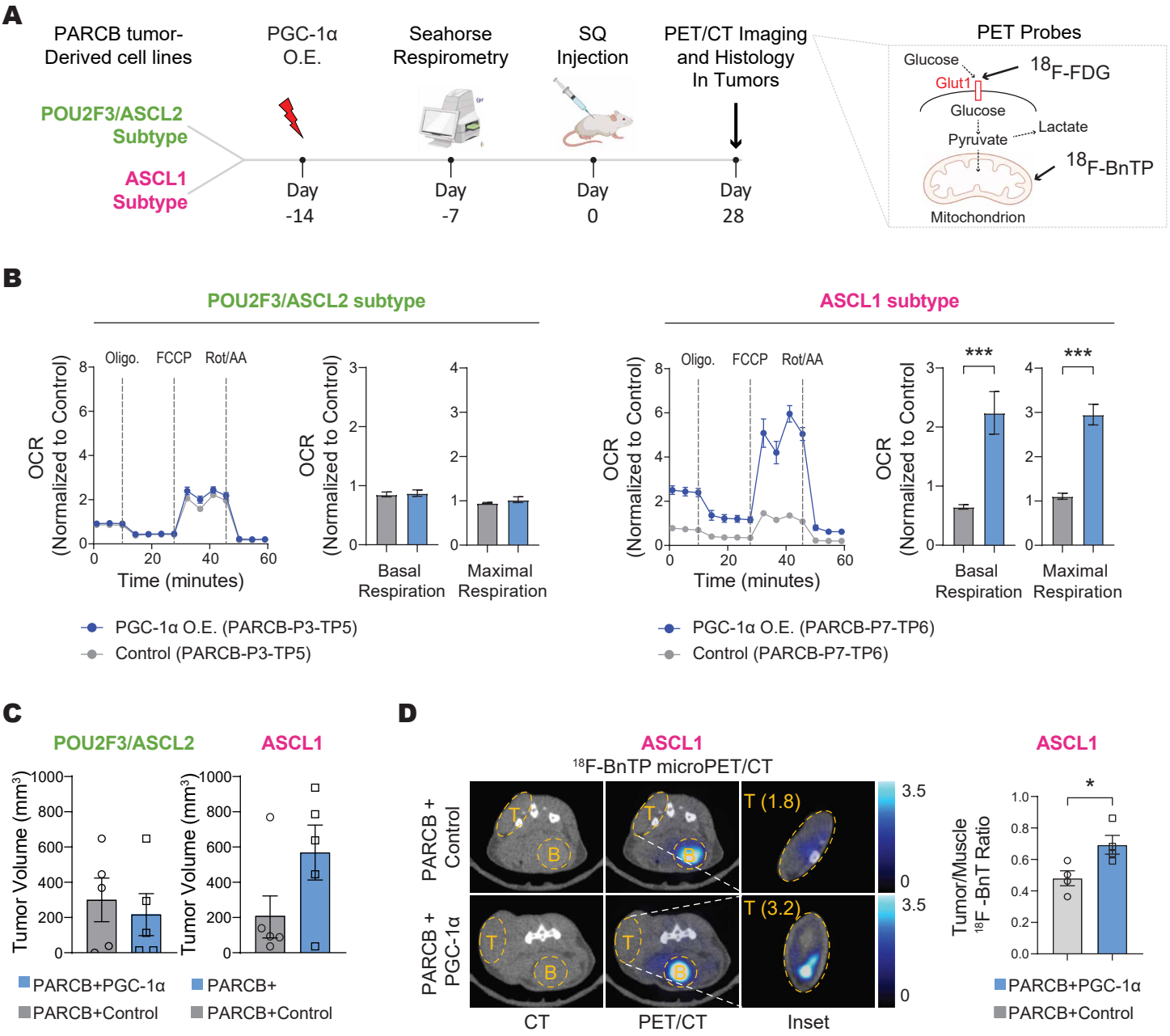
A
PARCB tumor-Derived cell lines
PGC-1α O.E.
Seahorse Respirometry
SQ Injection
PET/CT Imaging and Histology In Tumors
PET Probes
POU2F3/ASCL2 Subtype
ASCL1 Subtype
Day -14
Day -7
Day 0
Day 28
Glucose
Glut1
18F-FDG
Glucose
Lactate
Pyruvate
18F-BnTP
Mitochondrion
B
POU2F3/ASCL2 subtype
ASCL1 subtype
Oligo.
FCCP
Rot/AA
OCR (Normalized to Control)
Time (minutes)
Basal Respiration
Maximal Respiration
***
PGC-1α O.E. (PARCB-P3-TP5)
Control (PARCB-P3-TP5)
PGC-1α O.E. (PARCB-P7-TP6)
Control (PARCB-P7-TP6)
C
POU2F3/ASCL2
ASCL1
Tumor Volume (mm3)
PARCB+PGC-1α
PARCB+Control
PARCB+
PARCB+Control
D
ASCL1
18F-BnTP microPET/CT
PARCB + Control
PARCB + PGC-1α
T
B
T (1.8)
T (3.2)
3.5
0
CT
PET/CT
Inset
ASCL1
Tumor/Muscle 18F -BnT Ratio
*
PARCB+PGC-1α
PARCB+Control

878 **Figure 5.** PGC-1α overexpression promotes OXPHOS in the SCN prostate cancer ASCL1 subtype.

879 A. Left panel: overview of experimental strategy. Right panel: Details on the Positron Emission
880 Tomography (PET) probes utilized and their general mechanisms of action.

881 B. Seahorse respirometry in POU2F3/ASCL2 and ASCL1 PARCB tumor-derived cell lines. Oligo,
882 Oligomycin; FCCP, Carbonyl cyanide-p-trifluoromethoxy-phenylhydrazone; Rot/AA, rotenone /
883 antimycin A.

884 C. Caliper measurements of tumors initiated by subcutaneous injection of POU2F3/ASCL2 and
885 ASCL1 PARCB cell lines with PGC-1α overexpression versus control.

886 D. Left panel: Representative ^{18}F-FBnTP transverse PET-CT images of mice with subcutaneous
887 tumor implantation. Uptake of PET probe was measured as the maximum percentage of injected
888 dose per cubic centimeter (ID%/cc). Tumors are labeled "T", and bladders are labeled "B". The
889 inset has been contrast enhanced to show the relatively low uptake of this probe in subcutaneous
890 tumors, as reported previously[107]. Right panel: quantification of ^{18}F-BnTP uptake in the indicated
891 groups. Values are normalized to PET signal from adjacent skeletal muscle.

892

893 Data are presented as mean ± SEM, with *** indicating a p-value ≤0.001. The absence of asterisks
894 indicates that statistical significance of p≤0.05 was not reached. For statistical tests used, see Material
895 and Methods section.

896

897 Related data can be found in Figure S8.

Figure 6

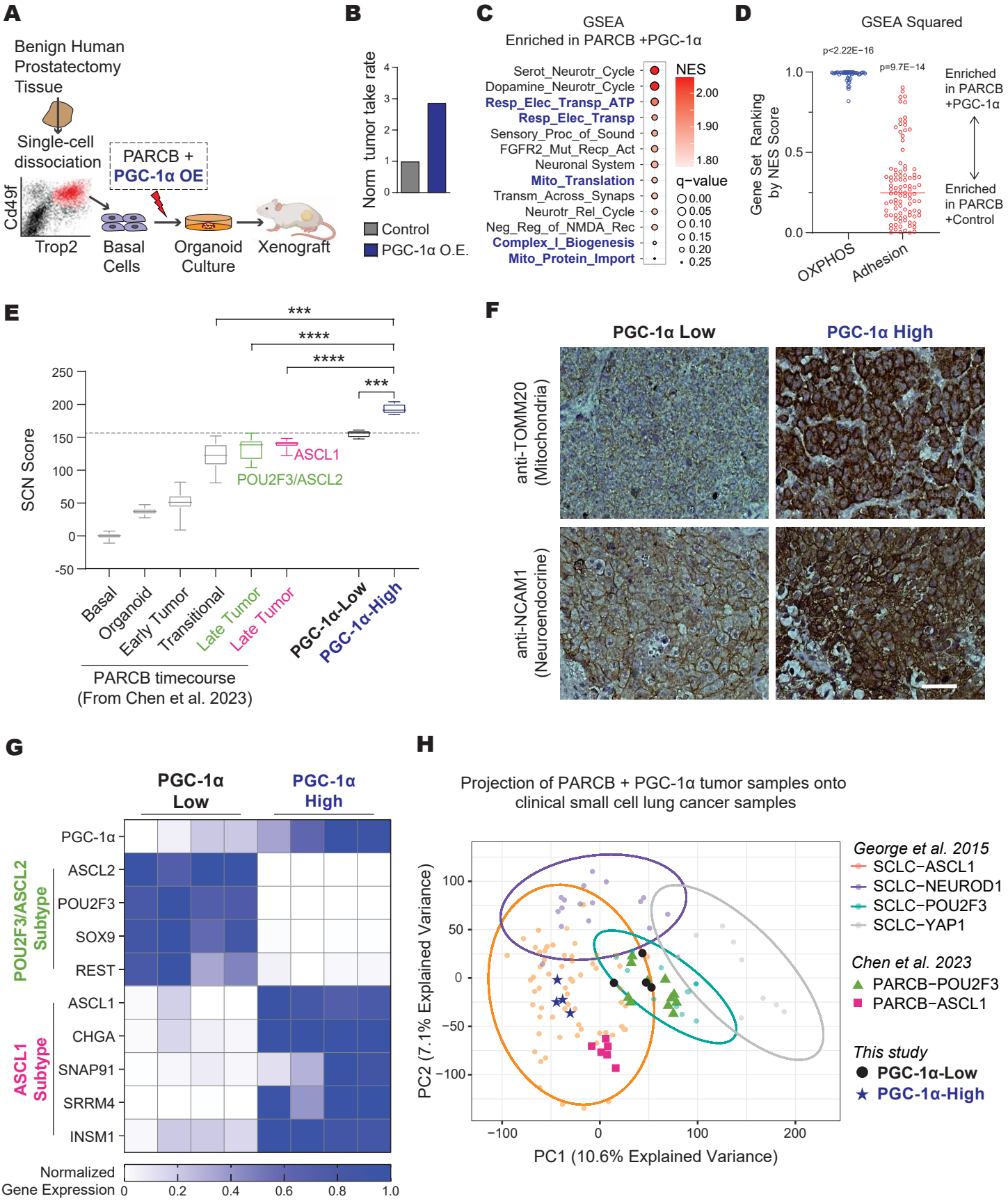
A
Benign Human Prostatectomy Tissue
Single-cell dissociation
PARCB + PGC-1α OE
Cd49f
Trop2
Basal Cells
Organoid Culture
Xenograft
B
Norm tumor take rate
Control
PGC-1α O.E.
C
GSEA
Enriched in PARCB +PGC-1α
Serot_Neurotr_Cycle
Dopamine_Neurotr_Cycle
Resp_Elec_Transp_ATP
Resp_Elec_Transp
Sensory_Proc_of_Sound
FGFR2_Mut_Recp_Act
Neuronal System
Mito_Translation
Transm_Across_Synaps
Neurotr_Rel_Cycle
Neg_Reg_of_NMDA_Rec
Complex_I_Biogenesis
Mito_Protein_Import
NES
q-value
D
GSEA Squared
p<2.22E-16
p=9.7E-14
Gene Set Ranking by NES Score
Enriched in PARCB +PGC-1α
Enriched in PARCB +Control
OXPHOS
Adhesion
E
SCN Score
ASCL1
POU2F3/ASCL2
Basal
Organoid
Early Tumor
Transitional
Late Tumor
Late Tumor
PGC-1α-Low
PGC-1α-High
PARCB timecourse
(From Chen et al. 2023)
F
PGC-1α Low
PGC-1α High
anti-TOMM20 (Mitochondria)
anti-NCAM1 (Neuroendocrine)
G
PGC-1α Low
PGC-1α High
PGC-1α
POU2F3/ASCL2 Subtype
ASCL2
POU2F3
SOX9
REST
ASCL1 Subtype
ASCL1
CHGA
SNAP91
SRRM4
INSM1
Normalized Gene Expression
H
Projection of PARCB + PGC-1α tumor samples onto clinical small cell lung cancer samples
PC2 (7.1% Explained Variance)
PC1 (10.6% Explained Variance)
George et al. 2015
SCLC−ASCL1
SCLC−NEUROD1
SCLC−POU2F3
SCLC−YAP1
Chen et al. 2023
PARCB−POU2F3
PARCB−ASCL1
This study
PGC-1α-Low
PGC-1α-High

898 **Figure 6.** PGC-1α overexpression upregulates OXPHOS and drives SCN prostate cancer towards an
899 ASCL1-expressing lineage.

900 A. Schematic illustrating the experimental setup for assessing the effects of PGC-1α overexpression
901 versus a control vector on PARCB-induced prostate cancer transformation.
902 B. Comparison of the tumor establishment rate ("tumor take rate") between PARCB transformation
903 using PGC-1α overexpression compared with control. PARCB transformations were performed
904 using three separate patient donors, resulting in a total of 45 xenografts being implanted in 23
905 mice.
906 C. GSEA in PARCB tumors with PGC-1α overexpression versus control.
907 D. GSEA squared analysis (described in the methods section and in reference[1]) depicting the
908 distribution of normalized enrichment scores (NES) for thousands of gene sets across multiple
909 gene set families in samples with PGC-1α overexpression versus control.
910 E. A transcriptomic analysis of SCN differentiation comparing SCN scores in PGC-1-High versus
911 PGC-1α-Low PARCB tumors. SCN scores (described in the methods section and in reference[1])
912 calculated from datasets derived from Chen et al 2023[11] are also shown for comparison.
913 F. Immunohistochemistry in histological sections derived from PARCB tumors with high and low
914 levels of PGC-1α.
915 G. A heatmap displaying normalized gene expression levels for signature genes related to
916 POU2F3/ASCL2 and ASCL1 tumor subtypes in PGC-1α-High versus PGC-1α-Low tumors.
917 H. Principal Component Analysis (PCA) of PARCB samples, distinguishing between PGC-1α-High
918 and PGC-1α-Low PARCB tumors from this study, overlaid on PARCB tumors from our prior time
919 course study[11] and SCLC cell lines from the CCLE and SCLC patient tumors from George et al.
920 2015[70].
921
922 Data in Figure 6E are presented as mean ± SEM, with statistical significance indicated by ****
923 ($p \leq 0.0001$) and *** ($p \leq 0.001$). For statistical tests used, see Material and Methods section.
924

Related data be can found in Figure S9.

REFERENCES

1. Balanis, N. G. *et al.* Pan-cancer Convergence to a Small-Cell Neuroendocrine Phenotype that Shares Susceptibilities with Hematological Malignancies. *Cancer Cell* **36**, 17-34.e7 (2019).
2. Park, J. W. *et al.* Reprogramming normal human epithelial tissues to a common, lethal neuroendocrine cancer lineage. *Science* **362**, 91–95 (2018).
3. Wang, L. *et al.* A genetically defined disease model reveals that urothelial cells can initiate divergent bladder cancer phenotypes. *Proceedings of the National Academy of Sciences* **117**, 563–572 (2020).
4. Oberg, K. *et al.* Consensus on biomarkers for neuroendocrine tumour disease. *The Lancet Oncology* **16**, e435–e446 (2015).
5. Nadal, R., Schweizer, M., Kryvenko, O. N., Epstein, J. I. & Eisenberger, M. A. Small cell carcinoma of the prostate. *Nat Rev Urol* **11**, 213–219 (2014).
6. Aggarwal, R. *et al.* Clinical and Genomic Characterization of Treatment-Emergent Small-Cell Neuroendocrine Prostate Cancer: A Multi-institutional Prospective Study. *JCO* **36**, 2492–2503 (2018).
7. Ireland, A. S. *et al.* MYC Drives Temporal Evolution of Small Cell Lung Cancer Subtypes by Reprogramming Neuroendocrine Fate. *Cancer Cell* **38**, 60-78.e12 (2020).
8. Sutherland, K. D., Ireland, A. S. & Oliver, T. G. Killing SCLC: insights into how to target a shapeshifting tumor. *Genes Dev* **36**, 241–258 (2022).
9. Brady, N. J. *et al.* Temporal evolution of cellular heterogeneity during the progression to advanced AR-negative prostate cancer. *Nat Commun* **12**, 3372 (2021).
10. Cejas, P. *et al.* Subtype heterogeneity and epigenetic convergence in neuroendocrine prostate cancer. *Nat Commun* **12**, 5775 (2021).
11. Chen, C.-C. *et al.* Temporal evolution reveals bifurcated lineages in aggressive neuroendocrine small cell prostate cancer trans-differentiation. *Cancer Cell* **41**, 2066-2082.e9 (2023).
12. Chan, J. M. *et al.* Lineage plasticity in prostate cancer depends on JAK/STAT inflammatory signaling. *Science* **377**, 1180–1191 (2022).
13. Mu, P. *et al.* SOX2 promotes lineage plasticity and antiandrogen resistance in TP53- and RB1-deficient prostate cancer. *Science* **355**, 84–88 (2017).
14. Gardner, E. E. *et al.* Lineage-specific intolerance to oncogenic drivers restricts histological transformation. *Science* **383**, eadj1415 (2024).
15. Huang, F. *et al.* Inosine Monophosphate Dehydrogenase Dependence in a Subset of Small Cell Lung Cancers. *Cell Metab* **28**, 369-382.e5 (2018).
16. Chalishazar, M. D. *et al.* MYC-Driven Small-Cell Lung Cancer is Metabolically Distinct and Vulnerable to Arginine Depletion. *Clinical Cancer Research* **25**, 5107–5121 (2019).
17. Zhang, C., Shang, X. & Wang, H. Untargeted metabolomics and lipidomics identified four subtypes of small cell lung cancer. *Metabolomics* **19**, 3 (2022).
18. Kim, J. & DeBerardinis, R. J. Mechanisms and implications of metabolic heterogeneity in cancer. *Cell Metab* **30**, 434–446 (2019).
19. Szeitz, B. *et al.* In-depth proteomic analysis reveals unique subtype-specific signatures in human small-cell lung cancer. *Clinical and Translational Medicine* **12**, e1060 (2022).
20. Nagarajan, A., Malvi, P. & Wajapeyee, N. Oncogene-Directed Alterations in Cancer Cell Metabolism. *Trends in Cancer* **2**, 365–377 (2016).
21. Folmes, C. D. L., Dzeja, P. P., Nelson, T. J. & Terzic, A. Metabolic Plasticity in Stem Cell Homeostasis and Differentiation. *Cell Stem Cell* **11**, 596–606 (2012).
22. Morrish, F. & Hockenbery, D. MYC and Mitochondrial Biogenesis. *Cold Spring Harb Perspect Med* **4**, a014225 (2014).
23. Chen, J. *et al.* MYC-driven increases in mitochondrial DNA copy number occur early and persist throughout prostatic cancer progression. *bioRxiv* 2023.02.20.529259 (2023) doi:10.1101/2023.02.20.529259.
24. Purhonen, J., Klefström, J. & Kallijärvi, J. MYC—an emerging player in mitochondrial diseases. *Frontiers in Cell and Developmental Biology* **11**, (2023).

979 25. Sancho, P. *et al.* MYC/PGC-1α Balance Determines the Metabolic Phenotype and Plasticity of
980 Pancreatic Cancer Stem Cells. *Cell Metabolism* **22**, 590–605 (2015).
981 26. Stine, Z. E., Walton, Z. E., Altman, B. J., Hsieh, A. L. & Dang, C. V. MYC, Metabolism, and Cancer.
982 *Cancer Discovery* **5**, 1024–1039 (2015).
983 27. Hoxhaj, G. & Manning, B. D. The PI3K–AKT network at the interface of oncogenic signalling and
984 cancer metabolism. *Nature Reviews Cancer* **20**, 74–88 (2020).
985 28. Whiteman, E. L., Cho, H. & Birnbaum, M. J. Role of Akt/protein kinase B in metabolism. *Trends in*
986 *Endocrinology & Metabolism* **13**, 444–451 (2002).
987 29. Zhang, C. *et al.* Tumour-associated mutant p53 drives the Warburg effect. *Nat Commun* **4**, 2935
988 (2013).
989 30. Aquilano, K. *et al.* p53 Orchestrates the PGC-1α-Mediated Antioxidant Response Upon Mild Redox
990 and Metabolic Imbalance. *Antioxid Redox Signal* **18**, 386–399 (2013).
991 31. Zacksenhaus, E. *et al.* Mitochondrial OXPHOS induced by RB1 deficiency in breast cancer:
992 implications for anabolic metabolism, stemness, and metastasis. *Trends in cancer* **3**, 768–779
993 (2017).
994 32. Conroy, L. R. *et al.* Loss of Rb1 enhances glycolytic metabolism in Kras-driven lung tumors in vivo.
995 *Cancers* **12**, 237 (2020).
996 33. Clem, B. F. & Chesney, J. Molecular pathways: regulation of metabolism by RB. *Clinical Cancer*
997 *Research* **18**, 6096–6100 (2012).
998 34. Warburg, O., Wind, F. & Negelein, E. THE METABOLISM OF TUMORS IN THE BODY. *J Gen*
999 *Physiol* **8**, 519–530 (1927).
1000 35. Warburg, O. On the origin of cancer cells. *Science* **123**, 309–314 (1956).
1001 36. Vander Heiden, M. G., Cantley, L. C. & Thompson, C. B. Understanding the Warburg Effect: The
1002 Metabolic Requirements of Cell Proliferation. *Science* **324**, 1029–1033 (2009).
1003 37. Faubert, B., Solmonson, A. & DeBerardinis, R. J. Metabolic reprogramming and cancer
1004 progression. *Science* **368**, eaaw5473 (2020).
1005 38. Vasan, K., Werner, M. & Chandel, N. S. Mitochondrial Metabolism as a Target for Cancer Therapy.
1006 *Cell Metabolism* **32**, 341–352 (2020).
1007 39. Vander Heiden, M. G. & DeBerardinis, R. J. Understanding the Intersections between Metabolism
1008 and Cancer Biology. *Cell* **168**, 657–669 (2017).
1009 40. Farge, T. *et al.* Chemotherapy-Resistant Human Acute Myeloid Leukemia Cells Are Not Enriched
1010 for Leukemic Stem Cells but Require Oxidative Metabolism. *Cancer Discovery* **7**, 716–735 (2017).
1011 41. Guièze, R. *et al.* Mitochondrial Reprogramming Underlies Resistance to BCL-2 Inhibition in
1012 Lymphoid Malignancies. *Cancer Cell* **36**, 369-384.e13 (2019).
1013 42. Viale, A. *et al.* Oncogene ablation-resistant pancreatic cancer cells depend on mitochondrial
1014 function. *Nature* **514**, 628–632 (2014).
1015 43. Bosc, C., Selak, M. A. & Sarry, J.-E. Resistance Is Futile: Targeting Mitochondrial Energetics and
1016 Metabolism to Overcome Drug Resistance in Cancer Treatment. *Cell Metabolism* **26**, 705–707
1017 (2017).
1018 44. Kuntz, E. M. *et al.* Targeting mitochondrial oxidative phosphorylation eradicates therapy-resistant
1019 chronic myeloid leukemia stem cells. *Nat Med* **23**, 1234–1240 (2017).
1020 45. Pendleton, K. E., Wang, K. & Echeverria, G. V. Rewiring of mitochondrial metabolism in therapy-
1021 resistant cancers: permanent and plastic adaptations. *Frontiers in Cell and Developmental Biology*
1022 **11**, (2023).
1023 46. Molina, J. R. *et al.* An inhibitor of oxidative phosphorylation exploits cancer vulnerability. *Nat Med*
1024 **24**, 1036–1046 (2018).
1025 47. Wheaton, W. W. *et al.* Metformin inhibits mitochondrial complex I of cancer cells to reduce
1026 tumorigenesis. *eLife* **3**, e02242 (2014).
1027 48. Evans, K. W. *et al.* Oxidative Phosphorylation Is a Metabolic Vulnerability in Chemotherapy-
1028 Resistant Triple-Negative Breast Cancer. *Cancer Research* **81**, 5572–5581 (2021).
1029 49. Choi, S. Y. C. *et al.* Targeting MCT4 to reduce lactic acid secretion and glycolysis for treatment of
1030 neuroendocrine prostate cancer. *Cancer Med* (2018) doi:10.1002/cam4.1587.

1031 50. Puigserver, P. & Spiegelman, B. M. Peroxisome Proliferator-Activated Receptor-γ Coactivator 1α
1032 (PGC-1α): Transcriptional Coactivator and Metabolic Regulator. *Endocrine Reviews* **24**, 78–90
1033 (2003).
1034 51. Puigserver, P. *et al.* A Cold-Inducible Coactivator of Nuclear Receptors Linked to Adaptive
1035 Thermogenesis. *Cell* **92**, 829–839 (1998).
1036 52. Luo, C., Widlund, H. R. & Puigserver, P. PGC-1 Coactivators: Shepherding the Mitochondrial
1037 Biogenesis of Tumors. *Trends in Cancer* **2**, 619–631 (2016).
1038 53. Tennakoon, J. B. *et al.* Androgens regulate prostate cancer cell growth via an AMPK-PGC-1α-
1039 mediated metabolic switch. *Oncogene* **33**, 5251–5261 (2014).
1040 54. Shiota, M. *et al.* Peroxisome proliferator-activated receptor gamma coactivator-1alpha interacts with
1041 the androgen receptor (AR) and promotes prostate cancer cell growth by activating the AR. *Mol*
1042 *Endocrinol* **24**, 114–127 (2010).
1043 55. Kaminski, L. *et al.* PGC1α Inhibits Polyamine Synthesis to Suppress Prostate Cancer
1044 Aggressiveness. *Cancer Research* **79**, 3268–3280 (2019).
1045 56. Valcarcel-Jimenez, L. *et al.* PGC1α Suppresses Prostate Cancer Cell Invasion through ERRα
1046 Transcriptional Control. *Cancer Research* **79**, 6153–6165 (2019).
1047 57. Torrano, V. *et al.* The metabolic co-regulator PGC1α suppresses prostate cancer metastasis. *Nat*
1048 *Cell Biol* **18**, 645–656 (2016).
1049 58. Vazquez, F. *et al.* PGC1α expression defines a subset of human melanoma tumors with increased
1050 mitochondrial capacity and resistance to oxidative stress. *Cancer Cell* **23**, 287–301 (2013).
1051 59. Luo, C. *et al.* A PGC1α-mediated transcriptional axis suppresses melanoma metastasis. *Nature*
1052 **537**, 422–426 (2016).
1053 60. Oh, T.-I. *et al.* PGC1α Loss Promotes Lung Cancer Metastasis through Epithelial-Mesenchymal
1054 Transition. *Cancers (Basel)* **13**, 1772 (2021).
1055 61. LeBleu, V. S. *et al.* PGC-1α mediates mitochondrial biogenesis and oxidative phosphorylation in
1056 cancer cells to promote metastasis. *Nat Cell Biol* **16**, 992–1003 (2014).
1057 62. Borges, M. *et al.* An achaete-scute homologue essential for neuroendocrine differentiation in the
1058 lung. *Nature* **386**, 852–855 (1997).
1059 63. Nouruzi, S. *et al.* ASCL1 activates neuronal stem cell-like lineage programming through remodeling
1060 of the chromatin landscape in prostate cancer. *Nat Commun* **13**, 2282 (2022).
1061 64. García-Bellido, A. & Santamaria, P. Developmental Analysis of the Achaete-Scute System of
1062 DROSOPHILA MELANOGASTER. *Genetics* **88**, 469–486 (1978).
1063 65. The Cancer Genome Atlas Program (TCGA) - NCI. https://www.cancer.gov/ccg/research/genome-
1064 sequencing/tcga (2022).
1065 66. Beltran, H. *et al.* Divergent clonal evolution of castration-resistant neuroendocrine prostate cancer.
1066 *Nat Med* **22**, 298–305 (2016).
1067 67. Abida, W. *et al.* Genomic correlates of clinical outcome in advanced prostate cancer. *Proceedings*
1068 *of the National Academy of Sciences* **116**, 11428–11436 (2019).
1069 68. Labrecque, M. P. *et al.* Molecular profiling stratifies diverse phenotypes of treatment-refractory
1070 metastatic castration-resistant prostate cancer. *J Clin Invest* **129**, 4492–4505 (2019).
1071 69. Beltran, H. *et al.* The Role of Lineage Plasticity in Prostate Cancer Therapy Resistance. *Clinical*
1072 *Cancer Research* **25**, 6916–6924 (2019).
1073 70. George, J. *et al.* Comprehensive genomic profiles of small cell lung cancer. *Nature* **524**, 47–53
1074 (2015).
1075 71. Cancer Genome Atlas Research Network. Integrated genomic analyses of ovarian carcinoma.
1076 *Nature* **474**, 609–615 (2011).
1077 72. Zhang, Y. *et al.* Androgen deprivation promotes neuroendocrine differentiation and angiogenesis
1078 through CREB-EZH2-TSP1 pathway in prostate cancers. *Nat Commun* **9**, 4080 (2018).
1079 73. Li, Y. *et al.* SRRM4 Drives Neuroendocrine Transdifferentiation of Prostate Adenocarcinoma Under
1080 Androgen Receptor Pathway Inhibition. *European Urology* **71**, 68–78 (2017).
1081 74. Rajan, P. *et al.* Next-generation Sequencing of Advanced Prostate Cancer Treated with Androgen-
1082 deprivation Therapy. *European Urology* **66**, 32–39 (2014).

1083 75. Augustyn, A. *et al.* ASCL1 is a lineage oncogene providing therapeutic targets for high-grade
1084 neuroendocrine lung cancers. *Proceedings of the National Academy of Sciences* **111**, 14788–
1085 14793 (2014).
1086 76. Borromeo, M. D. *et al.* ASCL1 and NEUROD1 Reveal Heterogeneity in Pulmonary Neuroendocrine
1087 Tumors and Regulate Distinct Genetic Programs. *Cell Rep* **16**, 1259–1272 (2016).
1088 77. Li, S. *et al.* Defined cellular reprogramming of androgen receptor-active prostate cancer to
1089 neuroendocrine prostate cancer. *Cell Reports* (In review).
1090 78. Jannig, P. R., Dumesic, P. A., Spiegelman, B. M. & Ruas, J. L. SnapShot: Regulation and biology
1091 of PGC-1α. *Cell* **185**, 1444-1444.e1 (2022).
1092 79. Divakaruni, A. S., Paradyse, A., Ferrick, D. A., Murphy, A. N. & Jastroch, M. Chapter Sixteen -
1093 Analysis and Interpretation of Microplate-Based Oxygen Consumption and pH Data. in *Methods in*
1094 *Enzymology* (eds. Murphy, A. N. & Chan, D. C.) vol. 547 309–354 (Academic Press, 2014).
1095 80. Bricker, D. K. *et al.* A Mitochondrial Pyruvate Carrier Required for Pyruvate Uptake in Yeast,
1096 Drosophila, and Humans. *Science* **337**, 96–100 (2012).
1097 81. Sharabi, K. *et al.* Selective Chemical Inhibition of PGC-1α Gluconeogenic Activity Ameliorates Type
1098 2 Diabetes. *Cell* **169**, 148-160.e15 (2017).
1099 82. Tsherniak, A. *et al.* Defining a Cancer Dependency Map. *Cell* **170**, 564-576.e16 (2017).
1100 83. Bonekamp, N. A. *et al.* Small-molecule inhibitors of human mitochondrial DNA transcription. *Nature*
1101 **588**, 712–716 (2020).
1102 84. Seo, B. B. *et al.* Molecular remedy of complex I defects: Rotenone-insensitive internal NADH-
1103 quinone oxidoreductase of Saccharomyces cerevisiae mitochondria restores the NADH oxidase
1104 activity of complex I-deficient mammalian cells. *Proceedings of the National Academy of Sciences*
1105 **95**, 9167–9171 (1998).
1106 85. Dart, A. Mapping out mitochondria. *Nat Rev Cancer* **23**, 273–273 (2023).
1107 86. Finck, B. N. & Kelly, D. P. PGC-1 coactivators: inducible regulators of energy metabolism in health
1108 and disease. *J Clin Invest* **116**, 615–622 (2006).
1109 87. Yap, T. A. *et al.* Phase I trial of IACS-010759 (IACS), a potent, selective inhibitor of complex I of the
1110 mitochondrial electron transport chain, in patients (pts) with advanced solid tumors. *JCO* **37**, 3014–
1111 3014 (2019).
1112 88. M.D. Anderson Cancer Center. *Phase 1 Study of IACS-010759 in Subjects With Relapsed or*
1113 *Refractory AML*. https://clinicaltrials.gov/ct2/show/NCT02882321 (2022).
1114 89. Tsuji, A., Akao, T., Masuya, T., Murai, M. & Miyoshi, H. IACS-010759, a potent inhibitor of
1115 glycolysis-deficient hypoxic tumor cells, inhibits mitochondrial respiratory complex I through a
1116 unique mechanism. *J Biol Chem* **295**, 7481–7491 (2020).
1117 90. Yap, T. A. *et al.* Complex I inhibitor of oxidative phosphorylation in advanced solid tumors and
1118 acute myeloid leukemia: phase I trials. *Nat Med* **29**, 115–126 (2023).
1119 91. Zhang, X. & Dang, C. V. Time to hit pause on mitochondria-targeting cancer therapies. *Nat Med* **29**,
1120 29–30 (2023).
1121 92. Miller, K. N., Clark, J. P. & Anderson, R. M. Mitochondrial regulator PGC-1α—Modulating the
1122 modulator. *Current Opinion in Endocrine and Metabolic Research* **5**, 37–44 (2019).
1123 93. Dominy, J. E. *et al.* The deacetylase Sirt6 activates the acetyltransferase GCN5 and suppresses
1124 hepatic gluconeogenesis. *Mol Cell* **48**, 900–913 (2012).
1125 94. Lerin, C. *et al.* GCN5 acetyltransferase complex controls glucose metabolism through
1126 transcriptional repression of PGC-1αlpha. *Cell Metab* **3**, 429–438 (2006).
1127 95. Xiang, Y. *et al.* SR18292 exerts potent antitumor effects in multiple myeloma via inhibition of
1128 oxidative phosphorylation. *Life Sci* **256**, 117971 (2020).
1129 96. Basu, H. S. *et al.* Prostate cancer cells survive anti-androgen and mitochondrial metabolic inhibitors
1130 by modulating glycolysis and mitochondrial metabolic activities. *Prostate* **81**, 799–811 (2021).
1131 97. Crowell, P. D. *et al.* MYC is a regulator of androgen receptor inhibition-induced metabolic
1132 requirements in prostate cancer. *Cell Rep* **42**, 113221 (2023).
1133 98. Love, M. I., Huber, W. & Anders, S. Moderated estimation of fold change and dispersion for RNA-
1134 seq data with DESeq2. *Genome Biol* **15**, 550 (2014).
1135 99. Liberzon, A. *et al.* Molecular signatures database (MSigDB) 3.0. *Bioinformatics* **27**, 1739–1740
1136 (2011).

1137 100. Subramanian, A. *et al.* Gene set enrichment analysis: a knowledge-based approach for
1138 interpreting genome-wide expression profiles. *Proc Natl Acad Sci U S A* **102**, 15545–15550 (2005).
1139 101. Quinlan, A. R. & Hall, I. M. BEDTools: a flexible suite of utilities for comparing genomic features.
1140 *Bioinformatics* **26**, 841–842 (2010).
1141 102. Ritchie, M. E. *et al.* limma powers differential expression analyses for RNA-sequencing and
1142 microarray studies. *Nucleic Acids Res* **43**, e47 (2015).
1143 103. Heinz, S. *et al.* Simple combinations of lineage-determining transcription factors prime cis-
1144 regulatory elements required for macrophage and B cell identities. *Mol Cell* **38**, 576–589 (2010).
1145 104. Hao, Y. *et al.* Dictionary learning for integrative, multimodal and scalable single-cell analysis.
1146 *Nat Biotechnol* **42**, 293–304 (2024).
1147 105. Han, M. *et al.* Spatial mapping of mitochondrial networks and bioenergetics in lung cancer.
1148 *Nature* **615**, 712–719 (2023).
1149 106. Sharp, A. *et al.* Clinical Utility of Circulating Tumour Cell Androgen Receptor Splice Variant-7
1150 Status in Metastatic Castration-resistant Prostate Cancer. *European Urology* **76**, 676–685 (2019).
1151 107. Momcilovic, M. *et al.* In vivo imaging of mitochondrial membrane potential in non-small-cell lung
1152 cancer. *Nature* **575**, 380–384 (2019).
1153 108. Szklarczyk, D. *et al.* The STRING database in 2023: protein-protein association networks and
1154 functional enrichment analyses for any sequenced genome of interest. *Nucleic Acids Res* **51**,
1155 D638–D646 (2023).

1156 **ACKNOWLEDGEMENTS**

1157 We thank the University of California, Los Angeles (UCLA) Tissue Procurement Core Laboratories
1158 for prostate tissue preparation and histological staining, and the UCLA Technology Center for Genomics
1159 and Bioinformatics for RNA sequencing. We thank Nicholas Bayley at UCLA for RNA-sequencing data
1160 processing. The microPET/CT imaging in this study was supported by the NIH Cancer Center Support
1161 Grant (2 P30 CA016042-44). The GNEXT PET/CT scanner was funded by NIH S10 Shared
1162 Instrumentation for Animal Research Grant (1 S10 OD026917-01A1). We thank Linsey Stiles and Katrina
1163 P. Montales of the UCLA Mitochondria and Metabolism Core for assistance with the XF96 Extracellular
1164 Flux Analyzer. The graphical abstract and Figure 2A were partially created with BioRender.com. Finally,
1165 we thank the following UCLA undergraduate research assistants who helped with wet lab experiments:
1166 Spencer Gaut, Alitzel Martinez, Michelle Garcia, and Kathy Rivera.

1167 Funding: The G. Harold and Leila Y. Mathers Charitable Foundation (O.N.W.). NIH UCLA SPORE
1168 in Prostate Cancer Grant P50CA092131 (O.N.W. and T.G.G.). NIH R01 Grant R01CA222877 (O.N.W.
1169 and T.G.G.), W. M. Keck Foundation Award 20182490 (O.N.W. and T.G.G.), UCLA Eli and Edythe Broad
1170 Center of Regenerative Medicine and Stem Cell Research Hal Gaba Director's Fund for Cancer Stem
1171 Cell Research (O.N.W. and T.G.G.). G.V. was supported by a Tumor Cell Biology Training Program NIH
1172 Grant (NIH T32 CA-009056). SM and GAD are partially supported by Veteran Affairs funds I01BX006019
1173 and I01BX004651 to SM. SM and GAD are also supported by UCLA Eli and Edythe Broad Center of
1174 Regenerative Medicine and Stem Cell Research Award, supported by the Binder Foundation to SM and
1175 TG. F.N.E. was supported by a University of California–Historically Black Colleges and Universities (UC–
1176 HBCU) Initiative Fellowship provided by University of California Office of the President (UCOP).

1177

1178 **AUTHOR CONTRIBUTIONS**

1179 Conceptualization: G.V., O.N.W.; Methodology: G.V., S.X., V.B., D.S., J.W.P., T.G., O.N.W.;
1180 Formal Analysis: G.V., C.C., J.F., T.H., W.T., K.S., M.H., F.N.E., L.W.; Investigation: G.V., D.C., V.B.,
1181 F.N.E., G.A.B.; Resources: C.C., J.W.P., S.M.; Writing - Original Draft: G.V.; Writing – review & editing:
1182 G.V., E.A., O.N.W.; Visualization: G.V.; S.X., M.H.; Supervision: S.M., D.S., J.K.L, T.G., O.S., O.N.W.

1183 **DECLARATION OF INTERESTS**

1184 O.N.W. currently has consulting, equity, and/or board relationships with Trethera Corporation,
1185 Kronos Biosciences, Sofie Biosciences, Breakthrough Properties, Vida Ventures, Nammi Therapeutics,
1186 Two River, Iconovir, Appia BioSciences, Neogene Therapeutics, 76Bio, and Allogene Therapeutics.
1187 J.K.L. has served as a consultant for Hierax Therapeutics and has equity in, an invention licensed to, and
1188 a sponsored research agreement with PromiCell Therapeutics. O.S.S. is a co-founder and SAB member
1189 of Enspire Bio LLC, Senergy-Bio and Capacity-Bio, and when this study was conducted, he was serving
1190 as a consultant to LUCA-Science. T.G.G. reports having consulting and equity agreements with Auron
1191 Therapeutics, Boundless Bio, Coherus BioSciences and Trethera Corporation. None of these companies
1192 contributed to or directed any of the research reported in this article.